SANDIA REPORT
SAND2022-0833
Printed January, 2022

Sandia National Laboratories

Quantifying the Impacts of Grain-scale Heterogeneity on Mechanical Response

Coleman Alleman

Prepared by
Sandia National Laboratories
Albuquerque, New Mexico 87185
Livermore, California 94550

Issued by Sandia National Laboratories, operated for the United States Department of Energy by National Technology & Engineering Solutions of Sandia, LLC.

Available to DOE and DOE contractors from

U.S. Department of Energy
Office of Scientific and Technical Information
P.O. Box 62
Oak Ridge, TN 37831

Telephone: (865) 576-8401
Facsimile: (865) 576-5728
E-Mail: reports@osti.gov
Online ordering: http://www.osti.gov/scitech

Available to the public from

U.S. Department of Commerce
National Technical Information Service
5301 Shawnee Road
Alexandria, VA 22312

Telephone: (800) 553-6847
Facsimile: (703) 605-6900
E-Mail: orders@ntis.gov
Online order: https://classic.ntis.gov/help/order-methods

ABSTRACT

Driven by the exceedingly high computational demands of simulating mechanical response in complex engineered systems with finely resolved finite element models, there is a critical need to optimally reduce the fidelity of such simulations. The minimum required fidelity is constrained by error tolerances on the simulation results, but error bounds are often impossible to obtain a priori. One such source of error is the variability of material properties within a body due to spatially non-uniform processing conditions and inherent stochasticity in material microstructure. This study seeks to quantify the effects of microstructural heterogeneity on component- and system-scale performance to aid in the choice of an appropriate material model and spatial resolution for finite element analysis.

ACKNOWLEDGMENT

The author would like to acknowledge the staff members who shared their insight into the approach and material models used here, including especially Jakob Ostien, John Emery, and Jay Foulk. Additional thanks to John Emery for providing feedback on the contents of this document. Thanks also to Brian Phung, who performed a number of simulations and parameter sensitivity studies that provided valuable context for the work presented here.

CONTENTS

LIST OF FIGURES

LIST OF TABLES

NOTATION

Variables

Symbol	Definition
$\underline{\underline{\sigma}}$	Cauchy stress tensor
$\underline{\underline{S}}$	Second Piola-Kirchhoff stress tensor (intermediate configuration)
$\underline{\underline{F}}$	Deformation gradient
$\underline{\underline{F}}^e$	Elastic deformation gradient
$\underline{\underline{F}}^p$	Plastic deformation gradient
$\underline{\underline{E}}^e$	Elastic Green-Lagrange strain
$\underline{\underline{C}}^e$	Elastic right Cauchy-Green deformation tensor
$\underline{\underline{I}}$	Second-order identity tensor
$\mathbb{C}$	Elastic stiffness tensor
$\underline{s}_0^\alpha$	Slip direction for slip system α in the reference configuration
$\underline{s}^\alpha$	Slip direction for slip system α in the current configuration
$\underline{n}_0^\alpha$	Slip plane normal for slip system α in the reference configuration
$\underline{n}^\alpha$	Slip plane normal for slip system α in the current configuration
$\underline{\underline{P}}_0^\alpha$	Schmid tensor for slip system α in the reference configuration
$\underline{\underline{P}}^\alpha$	Schmid tensor for slip system α in the current configuration
$\underline{\underline{L}}$	Velocity gradient
$\underline{\underline{L}}^e$	Elastic velocity gradient
$\underline{\underline{L}}^p$	Plastic velocity gradient
$\underline{\underline{L}}^{p*}$	Plastic velocity gradient in the intermediate configuration
$\dot{\gamma}^\alpha$	Slip rate on slip system α
g^α	Slip resistance for slip system α
τ^α	Resolved shear stress on slip system α
$\underline{\underline{\tau}}$	Kirchhoff stress
$\underline{e}_i$	Orthonormal basis vector
$\underline{\underline{R}}$	Orientation tensor

Variables (continued)

Symbol	Definition
$\mathbb{A}$	Strain concentration tensor
c_k	Volume fraction of constituent phase k
$\underline{\underline{\bar{\mathrm{E}}}}$	Average elastic strain
$\underline{\underline{\tilde{\mathrm{E}}}}$	Deviation from average elastic strain
$\underline{\underline{\Lambda}}$	Eigenstrain tensor
$\mathbb{S}$	Eshelby tensor
$\mathbb{T}$	Interaction tensor
ϕ_1	First Bunge euler angle
Φ	Second Bunge euler angle
ϕ_2	Third Bunge euler angle
$\mathbb{P}$	Orthonormal fourth-order tensor basis
$\mathbb{E}$	Fourth-order tensor basis with cubic symmetry
W^e	Elastic strain energy
C_Δ	Cubic anisotropy factor
A	Zener anisotropy ratio
α	Anisotropy measure
L	Spatial length scale
d_g	Average grain size (diameter)
d^p	Pointwise plastic dissipation
$\mathcal{D}^p$	Total plastic dissipation
J	Determinant of the deformation gradient
τ	Equivalent Kirchhoff stress
$\underline{\underline{\mathrm{n}}}$	Stress direction
f^α	Schmid factor
r	Stress-space radial coordinate
θ	Lode angle
t	Time
$\dot{\varepsilon}^p$	Equivalent plastic strain rate
μ	Shear modulus
I_i	Invariant of the Cauchy stress tensor
J_i	Invariant of the deviatoric stress tensor
$\mathbb{Y}$	Fourth-order yield tensor
s_i	Principal deviatoric stress
τ^{cr}	Critical resolved shear stress

Mathematical functions

Symbol	Definition
$\square^T$	Transpose of a tensor
$\|\square\|$	Frobenius norm of a tensor
$\mathrm{dev}(\square)$	Deviatoric part of a tensor
$\mathrm{tr}(\square)$	Trace of a tensor
$\dot{\square}$	Time derivative
$\det(\square)$	Determinant of a tensor
$\square \otimes \square$	Dyadic product
$\square \cdot \square$	Dot product
$\square : \square$	Double dot product

Material model parameters

Symbol	Definition
k	Inverse rate sensitivity
$\dot{\gamma}_0$	Reference slip rate
H	Hardening modulus
R_d	Dynamic recovery rate constant
g_0	Initial slip resistance
C_{11}	Cubic elastic constant
C_{12}	Cubic elastic constant
C_{44}	Cubic elastic constant
Y	Yield strength
n	Hosford exponent

1. BACKGROUND

The mechanical behavior of structural metals is ultimately determined by atomic scale interactions of constituents arranged in a crystal lattice populated with defects. Simulation of these interactions requires resolution of length scales down to 10^{-10} meters and timescales down to 10^{-15} seconds. Given these requirements it is generally infeasible to model engineering scale components and systems with atomic resolution. To circumvent this problem of computational intractability, the focus here is simulations of mechanical response with partial differential equations defined on a continuum. For all but perhaps the most extreme modes of deformation (such as shock loading) and strongly nonlinear processes (such as fracture), the continuum approach is sufficient to deliver simulations of mechanical response to within error tolerances well below those required for engineering calculations.

Approaches based on continuum mechanics are widely successful in engineering analysis, but a question that must be answered for each individual analysis concerns the level of detail that is required to capture the constitutive response of the material being deformed. When using a continuum model for structural alloys, the lowest level of detail typically simulated is the crystal grain, a region of uniform lattice orientation with length scales on the order of 10^{-6} meters. The analysis of a millimeter-scale component with this level of detail would require on the order of one billion finite elements, which is not reasonable for informing decision-making in a product design cycle. Thus, the nearly universal approach is to treat the continuum at an engineering scale for analysis, driving the resolution of lower length scales up to the point where the simulation of components becomes feasible, typically 10^{-3} meters and above.

The strategy of employing millimeter length scales in analysis is successful because the aggregated behavior of the underlying heterogeneous microstructure typically takes on a uniform and scale independent form at lengths at least an order of magnitude below the analysis resolution. Unfortunately, the terms ‘typically’ and ‘at least’ take on real significance in regions of stress concentration and strain localization, exactly where models of failure require additional detail to function as predictive tools. In these regions, accurate accounting of energy dissipation due to plasticity and damage mechanisms becomes critically important to delivering robust and meaningful predictions of the limits of material strength and ductility. In the absence of sufficient information, analysis can become non-conservative, and the lack of certainty around these calculations drives sub-optimal designs to achieve confidence around required performance.

Driven by the exceedingly high computational demands of finely resolved finite element models for simulation of the mechanical response of complex engineered systems, there is a critical need to optimally reduce the fidelity of such simulations. The minimum required fidelity is constrained by error tolerances on the simulation results, but error bounds are often impossible to obtain a

priori. Mesh refinement studies are commonplace in the optimization of a finite element mesh to reduce geometric resolution while retaining solution accuracy. On the constitutive side, however, this type of study is much harder to implement due to the labor-intensive process of model calibration and limited software implementation of models of variable complexity. These two limitations are being addressed by implementing algorithmic solutions for model calibration and software design incorporating modular treatment of the various pieces of the constitutive framework for plasticity and damage. This complementary effort seeks to quantify the effects of microstructural heterogeneity through relating, for example, material and geometric length scales to macroscale features of material response such as yield strength.

There are a number of ways to perform an assessment of microscale effects, including multiscale modeling methods that rely on either coupled calculations of multiple scales during a single simulation, or decoupled calculations that sample databases of micromechanical behavior [1]. In contrast, the focus here is on methods for producing closed-form expressions that return homogenized, macroscopic material behavior as a function of microstructural descriptors. The goal in deriving such methods is to provide a path to insert micromechanics into typical material models with a minimal increase in computational cost. This increase in cost is offset by the possibility of deploying rigorous, quantitative analyses to estimate uncertainty in model predictions. In addition, the results presented here include estimates of the diminution of micromechanical effects at larger length scales, providing practical guidance on when and to what degree a simulation-based prediction is uncertain with respect to microscale heterogeneity. For example, the analysis presented here suggests that anisotropic material behavior is observable even for nominally isotropic materials for length scales approaching 100μm. Thus, finite element analysis requiring 100μm spatial resolution cannot proceed with confidence until an assessment of the microstructural effects is made. These results, relating material microstructure to system-scale performance, aid in the choice of the appropriate material model for given loading scenarios and geometries relevant to the analysis of the mechanical response of engineering systems, thus giving analysts practical guidance for model selection and evaluation.

In this study, the focus is on the micromechanics of elasticity and plasticity in crystalline materials. In this context, ‘microstructure’ is taken to refer exclusively to grain morphology and orientation, which are known to significantly affect elastic and plastic anisotropy in structural metals. Grain morphology and orientation distributions can vary widely across engineering alloys and product forms. Here we consider a limited subset of this variation, employing nominally equiaxed grain geometries and sampling uniform orientation distributions. This largely ignores the effects of distorted grain shapes and non-uniform texture, which can result from processing such as rolling, but the conclusions and methodology remain informative. The approach is detailed in Section 2, followed by a presentation of some results on elasticity in Section 3.1 and on plasticity in Section 3.2.

2. APPROACH

In order to deliver better-functioning engineering scale models and analyses, this study seeks to quantify microscale uncertainty inherent in the analysis for a dual purpose: 1) Proper quantification allows improvement in designs by driving down the factor of safety required to achieve specified margins; 2) Identification of scenarios with unacceptable levels of uncertainty enables application of more detailed models within a limited spatial or temporal scope to drive down the inherent uncertainty in the calculation with an acceptable increase in computational cost.

In the current scope, attention is focused on two key aspects of material behavior, anisotropy and lode-angle-dependence. At the sub-grain scale (microscale), the material behavior is always anisotropic, and the amount of anisotropy varies widely among structural alloys. At the engineering scale (macroscale), the material behavior of structural alloys is mostly considered to be isotropic. This assumption is invalidated in two key ways: 1) The material is 'textured', meaning that processing conditions have produced a microstructure where the crystal lattice has a preferred orientation; 2) The length scale of the deformation is of similar order to the grain size, for example due to large gradients near stress concentrators. In the first case, mesoscale modeling can be used to determine parameter values for anisotropic material models from microstructural information, supplementing uniaxial test data and eliminating the need for additional testing. In the second case, mesoscale modeling can be used to inform the choice of an anisotropic model where required due to the nature of the analysis. In this way, mesoscale modeling is the bridge between expensive, accurate microscale modeling and inexpensive, approximate macroscale modeling.

In addition to the assumption of isotropy, the assumption of lode-angle-independence is often made in engineering analyses. Under this assumption, constitutive models are unable to properly account for differences in yield behavior for uniaxial, shear, and bi- or triaxial stress states with equal equivalent (von Mises) stress. It is well-known that this assumption is violated for some structural alloys even at the engineering scale, and it is violated to some degree for all structural materials at the microstructural scale. Mesoscale modeling can be used to probe deviations from the assumption of lode-angle-independence and quantify the effects on energy dissipation for loading paths of interest. A practical implication of this type of investigation is criteria for the selection of the appropriate yield surface and flow rule and their parametrization, as suggested by the results presented in Section 3.2.3.

Various aspects of the effects of microscale heterogeneity have been studied extensively in the literature. One such study [2], [3], found two effects that are especially relevant to the current study. First, the authors found that while a macroscale model accurately reproduced the mean

stress found in the microscale simulation, the macroscale model under-predicted the mean strain [2]. Second, the macroscale model over-predicted the stress near a mild geometric stress-concentrator, compared with the microscale model [3]. Part of the thrust of the current study is to extend the understanding gained in these previous two efforts by quantifying these effects as functions of microstructural and structure geometry parameters. This is important to studying localization preceding damage, which is governed as much or more by the extreme values as the mean values of the mechanical fields. The long-term impact of the current study will be realized when these analyses are applied to study the impact on simulations of mechanical behavior in realistic scenarios.

To study the relationships between the aggregated response of a microscale model and the best-fit macroscale model requires first interrogating an ensemble of microstructural configurations and extracting a volume-averaged response. Second, the response of the microscale model must be analyzed in terms of deriving optimal macroscale model parameters. Last, scaling of the response with various microstructural descriptors must be determined in order to provide a direct link between the microstructural descriptors and the parameter values for the macroscale model.

2.1. Microscale Constitutive Model

This study focuses on the micromechanics of crystalline solids, with particular emphasis on materials with cubic symmetry, with some specific focus on austenitic stainless steel, which has a face-centered cubic (FCC) crystal lattice. The material model, detailed below, has three essential features: hyperelasticity based on the Green-Lagrange strain, power-law viscoplasticity, and a saturating nonlinear strain hardening model.

2.1.1. Crystal Elasticity

The kinematics of the crystal elasto-plasticity model is based on a well-established continuum formulation and follows multiplicative decomposition of the deformation gradient. The total deformation gradient $\underline{\underline{F}}$ is decomposed into elastic and plastic parts.

$$\underline{\underline{F}} = \underline{\underline{F}}^e \cdot \underline{\underline{F}}^p \tag{2.1}$$

Here, $\underline{\underline{F}}^e$ and $\underline{\underline{F}}^p$ are the elastic and plastic part of the total deformation gradient, respectively. The elastic Green-Lagrange strain is given in terms of $\underline{\underline{F}}^e$ as

$$\underline{\underline{E}}^e = \frac{1}{2}\left(\underline{\underline{F}}^{e\mathrm{T}} \cdot \underline{\underline{F}}^{e\mathrm{T}} - \underline{\underline{I}}\right) = \frac{1}{2}\left(\underline{\underline{C}}^e - \underline{\underline{I}}\right) \tag{2.2}$$

where $\underline{\underline{C}}^e$ is the elastic right Cauchy-Green deformation tensor. The elastic constitutive law relates the second Piola-Kirchhoff stress in the intermediate configuration to the elastic Lagrangian strain as

$$\underline{\underline{S}} = \mathbb{C} : \underline{\underline{E}}^e \tag{2.3}$$

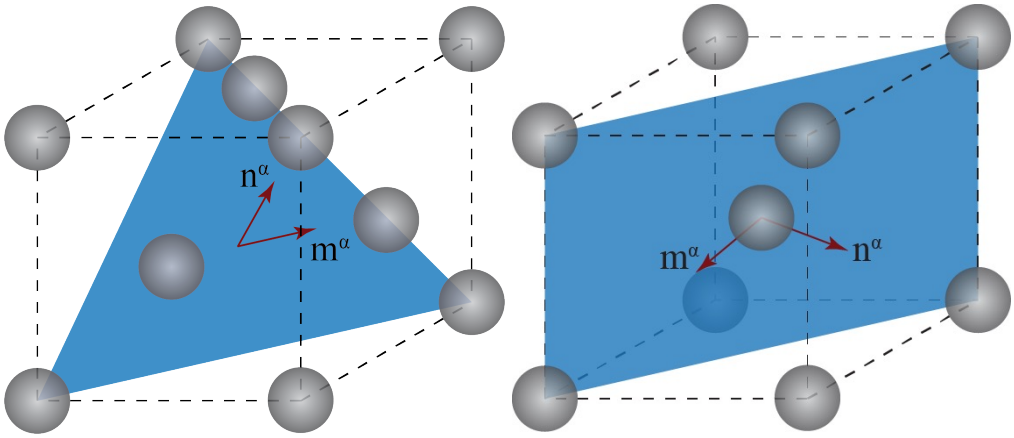

Figure 2-1. Slip system configurations within a unit cell for FCC (left) and BCC (right) crystal lattices.

where $\mathbb{C}$ is the elastic stiffness tensor. Solving Equation (2.1) for $\underline{\underline{F}}^e$,

$$\underline{\underline{F}}^e = \underline{\underline{F}} \cdot \left(\underline{\underline{F}}^p\right)^{-1} \tag{2.4}$$

it is seen that the stress $\underline{\underline{S}}$ can be obtained for a given $\underline{\underline{F}}$, given a solution for $\underline{\underline{F}}^p$. The plastic constitutive relations developed in the following section produce a set of equations to obtain $\underline{\underline{F}}^p$ for a given $\underline{\underline{F}}^e$, forming a coupled set of equations. The solution to these equations is a split of $\underline{\underline{F}}$ into $\underline{\underline{F}}^e$ and $\underline{\underline{F}}^p$ such that Equation (2.1) holds.

2.1.2. Crystal Plasticity

Here, crystal viscoplasticity is modeled as the collective effect of dislocations gliding on well-defined slip systems defined by a slip direction, $\underline{s}$, and a slip plane normal, $\underline{n}$. A typical model includes 12 $\{111\}\langle 110\rangle$ slip systems for FCC materials and 24 $\{110\}\langle 111\rangle$ slip systems for BCC materials, as depicted in Figure 2-1 and listed in Table 2-1. The Schmid tensor in the reference configuration, and in the intermediate configuration, assuming $\underline{\underline{F}}^p$ does not change the slip geometry, is

$$\underline{\underline{P}}_0^\alpha = \underline{s}_0^\alpha \otimes \underline{n}_0^\alpha \tag{2.5}$$

Here, $\underline{s}_0^\alpha$ and $\underline{n}_0^\alpha$ are the initial unit vectors in the slip direction and the slip plane normal direction on α-th slip system, respectively. As the crystal deforms, lattice is stretched and rotated according to $\underline{\underline{F}}^e$. Therefore, the slip direction and slip plane normal of the slip system α in the current configuration are given by

$$\begin{aligned} \underline{s}^\alpha &= \underline{\underline{F}}^e \cdot \underline{s}_0^\alpha \\ \underline{n}^\alpha &= \left(\underline{\underline{F}}^e\right)^{-\mathrm{T}} \cdot \underline{n}_0^\alpha \end{aligned} \tag{2.6}$$

Table 2-1. 12 FCC and 24 BCC slip systems.

Twelve FCC slip systems

α	System	α	System	α	System	α	System
1	$(\bar{1}10)[111]$	4	$(\bar{1}\bar{1}0)[\bar{1}11]$	7	$(1\bar{1}0)[\bar{1}\bar{1}1]$	10	$(110)[1\bar{1}1]$
2	$(0\bar{1}1)[111]$	5	$(101)[\bar{1}11]$	8	$(011)[\bar{1}\bar{1}1]$	11	$(\bar{1}01)[1\bar{1}1]$
3	$(10\bar{1})[111]$	6	$(01\bar{1})[\bar{1}11]$	9	$(\bar{1}0\bar{1})[\bar{1}\bar{1}1]$	12	$(0\bar{1}\bar{1})[1\bar{1}1]$

Twenty-four BCC slip systems

α	System	α	System	α	System	α	System
1	$(01\bar{1})[111]$	7	$(0\bar{1}\bar{1})[\bar{1}\bar{1}1]$	13	$(01\bar{1})[\bar{1}\bar{1}\bar{1}]$	19	$(0\bar{1}\bar{1})[11\bar{1}]$
2	$(\bar{1}01)[111]$	8	$(101)[\bar{1}\bar{1}1]$	14	$(\bar{1}01)[\bar{1}\bar{1}\bar{1}]$	20	$(101)[11\bar{1}]$
3	$(1\bar{1}0)[111]$	9	$(\bar{1}10)[\bar{1}\bar{1}1]$	15	$(1\bar{1}0)[\bar{1}\bar{1}\bar{1}]$	21	$(\bar{1}10)[11\bar{1}]$
4	$(\bar{1}0\bar{1})[\bar{1}11]$	10	$(10\bar{1})[1\bar{1}1]$	16	$(\bar{1}0\bar{1})[1\bar{1}\bar{1}]$	22	$(10\bar{1})[\bar{1}1\bar{1}]$
5	$(0\bar{1}1)[\bar{1}11]$	11	$(011)[1\bar{1}1]$	17	$(0\bar{1}1)[1\bar{1}\bar{1}]$	23	$(011)[\bar{1}1\bar{1}]$
6	$(110)[\bar{1}11]$	12	$(\bar{1}\bar{1}0)[1\bar{1}1]$	18	$(110)[1\bar{1}\bar{1}]$	24	$(\bar{1}\bar{1}0)[\bar{1}1\bar{1}]$

From the definitions in Equation (2.6), the Schmid tensor in the current configuration is

$$\underline{\underline{P}}^{\alpha} = \underline{s}^{\alpha} \otimes \underline{n}^{\alpha} = \underline{\underline{F}}^{e} \cdot \underline{\underline{P}}_{0}^{\alpha} \cdot \left(\underline{\underline{F}}^{e}\right)^{-1} \tag{2.7}$$

The velocity gradient, $\underline{\underline{L}}$ in the current configuration is written as:

$$\underline{\underline{L}} = \underline{\underline{L}}^{e} + \underline{\underline{L}}^{p} = \dot{\underline{\underline{F}}} \cdot \underline{\underline{F}}^{-1} \tag{2.8}$$

where, $\underline{\underline{L}}^{e}$ and $\underline{\underline{L}}^{p}$ are elastic and plastic parts of the velocity gradient, respectively, and can be represented as follows:

$$\underline{\underline{L}}^{e} = \dot{\underline{\underline{F}}}^{e} \cdot (\underline{\underline{F}}^{e})^{-1} \tag{2.9}$$

$$\underline{\underline{L}}^{p} = \underline{\underline{F}}^{e} \cdot \underline{\underline{L}}^{p*} \cdot (\underline{\underline{F}}^{e})^{-1} \tag{2.10}$$

Here, the plastic part of the velocity gradient in the intermediate configuration is given by

$$\underline{\underline{L}}^{p*} = \dot{\underline{\underline{F}}}^{p} \cdot (\underline{\underline{F}}^{p})^{-1} \tag{2.11}$$

Assuming plastic deformation is caused by the dislocation slip, the plastic part of the velocity gradient can be written in the current configuration as:

$$\underline{\underline{L}}^{p} = \sum_{\alpha} \dot{\gamma}^{\alpha} \underline{s}^{\alpha} \otimes \underline{n}^{\alpha} = \sum_{\alpha} \dot{\gamma}^{\alpha} \underline{\underline{P}}^{\alpha} \tag{2.12}$$

or, in the intermediate configuration as

$$\underline{\underline{L}}^{p*} = \sum_{\alpha} \dot{\gamma}^{\alpha} \underline{s}_{0}^{\alpha} \otimes \underline{n}_{0}^{\alpha} = \sum_{\alpha} \dot{\gamma}^{\alpha} \underline{\underline{P}}_{0}^{\alpha} \tag{2.13}$$

where $\dot{\gamma}^\alpha$ is the slip rate on slip system α. Combining Equations (2.11) and (2.13), a governing equation for $\underline{\underline{F}}^p$ is derived:

$$\dot{\underline{\underline{F}}}^p = \underline{\underline{L}}^{p*} \cdot \underline{\underline{F}}^p = \left(\sum_\alpha \dot{\gamma}^\alpha \underline{\underline{P}}_0^\alpha \right) \cdot \underline{\underline{F}}^p \tag{2.14}$$

It is noted that in this form, an $\underline{\underline{F}}^p$ that is initially isochoric ($\det(\underline{\underline{F}}^p) = 1$) will remain isochoric throughout the deformation. Care must be taken in the numerical solution of this equation to preserve this feature of $\underline{\underline{F}}^p$.

The critical aspect of the single crystal constitutive equations in crystal plasticity model is how the slip rate is related to the applied stress. One of the most widely used forms for a viscoplasticity model is the power-law function:

$$\dot{\gamma}^\alpha = \dot{\gamma}_0^\alpha \left| \frac{\tau^\alpha}{g^\alpha} \right|^k \operatorname{sign}(\tau^\alpha) \tag{2.15}$$

Here, $\dot{\gamma}_0^\alpha$ is the reference shear rate, k is the inverse rate sensitivity factor, and g^α is the slip resistance on slip system α. Assuming isochoric plasticity, the driving force τ^α for slip on system α is

$$\tau^\alpha = \det(\underline{\underline{F}}^e)\, \underline{\underline{\sigma}} : \underline{\underline{P}}^\alpha = \underline{\underline{C}}^e \cdot \underline{\underline{S}} : \underline{\underline{P}}_0^\alpha \tag{2.16}$$

2.1.3. Strain hardening

The slip resistance g^α on a slip system α evolves according to the following rule

$$\dot{g}^\alpha = \left(H - R_d g^\alpha \right) \dot{\gamma} \tag{2.17}$$

where H is the hardening modulus, R_d is the rate constant for dynamic recovery, and $\dot{\gamma}$ is the total slip rate over all slip systems,

$$\dot{\gamma} = \sum_{\alpha=1}^{N_{ss}} |\dot{\gamma}^\alpha| \tag{2.18}$$

This model results in a saturating hardening behavior with an asymptotic value of g^α,

$$g^\alpha (t \to \infty) = \frac{H}{R_d} \tag{2.19}$$

For a constant slip rate, $\dot{\gamma}$, Equation (2.17) has a closed-form solution,

$$g^\alpha (t) = \frac{H}{R_d} + \left(g_0 - \frac{H}{R_d} \right) \exp\left(-R_d \dot{\gamma} t \right) \tag{2.20}$$

This illustrates the saturation of the strain hardening via exponential decay, and serves as a useful tool in the numerical integration of (2.17), where a constant slip rate is assumed during a single timestep.

The model presented in this section is a useful tool for simulating the response of a material region with a single crystal orientation and no variation in the relevant mechanical fields. However, most engineering materials are composed of polycrystalline aggregates with spatially varying orientation, and most engineering designs are subjected to spatially varying mechanical fields during service. Therefore, it is necessary to generalize the model for realistic application. The simplest path to this generalization is to apply the single crystal model at each point in a domain, and solve the governing equations of mechanical equilibrium using, for example, the finite element method applied with an element-wise specification of material orientation. Numerous examples of this approach exist in the literature, but this path is computationally intractable for typical components and systems with sizes of centimeters to meters. For these applications, a model is required with drastically reduced detail in the treatment of the crystal mechanics. In the following sections, a number of homogenization techniques are applied to extract macroscale material behavior from detailed microscale descriptions of polycrystalline materials without the need for direct numerical simulation (DNS) of the microscale.

3. RESULTS

In a model of crystalline material, the spatial variation in the initial material state is commonly taken to be determined solely by the spatial variation of the orientation of the crystal lattice. This orientation is commonly defined as a tensor, $\underline{\underline{\mathrm{R}}}$, that maps the laboratory (spatial) basis to the material basis:

$$\underline{e}_i^{material} = \underline{\underline{\mathrm{R}}} \cdot \underline{e}_i^{spatial} \tag{3.1}$$

For example, in a face-centered-cubic material, the material basis is defined with respect to the crystal lattice as shown in Figure 3-1. In a polycrystalline aggregate, grains are defined as regions with uniform orientation:

$$G_i = \left\{ \underline{X} : \underline{\underline{\mathrm{R}}}\left(\underline{X}\right) = \underline{\underline{\mathrm{R}}}_i \right\} \tag{3.2}$$

A typical grain morphology is shown in Figure 3-2. The main problem of homogenization in this context is to derive effective material properties that represent the combined behavior of such aggregates via an appropriate scheme to accumulate the pointwise material properties of the constituents. This problem is treated separately for the elastic and plastic responses of a polycrystalline material in the following.

3.1. Homogenized elasticity

For models that represent the elastic behavior of a material via Equation (2.3), the problem of homogenizing the elastic response of a polycrystalline aggregate reduces to accumulating the elastic response to construct an effective elastic tensor, $\mathbb{C}_{\mathrm{eff}}$ from the constituent elastic tensors $\mathbb{C}_k$. Typically, the constituent tensors are identically defined with reference to the material basis, but their components in the spatial basis vary due to differences in material orientation. In general, the components of $\mathbb{C}$ in the spatial basis, $C_{ijkl}^{spatial}$ are then given in terms of the components in the the material basis, $C_{mnpq}^{material}$, by

$$C_{ijkl}^{spatial} = R_{im} R_{jn} R_{kp} R_{lq} C_{mnpq}^{material} \tag{3.3}$$

The problem is then to construct the components of the effective elastic tensor in the spatial basis from the spatial components of the constituent tensors. A number of methods to do this are summarized in the following.

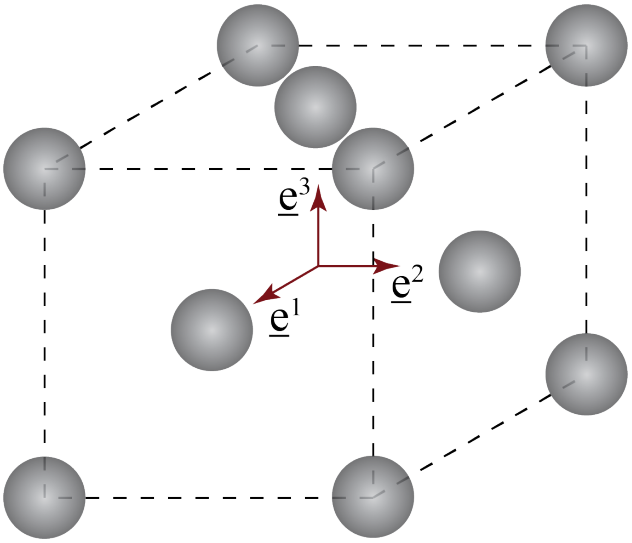

Figure 3-1. The unit cell for an FCC material, along with the canonical material basis.

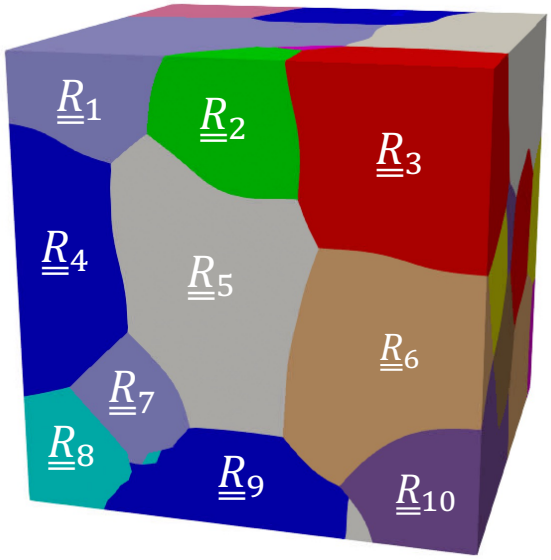

Figure 3-2. A polycrystalline aggregate is comprised of a number of grains, defined as regions of uniform crystal orientation.

3.1.1. Approximation of the Effective Elasticity Tensor

In a region k of a composite material with uniform elastic properties, the elastic constitutive relation given by Equation (2.3) is specified by

$$\underline{\underline{\mathrm{S}}}_k = \mathbb{C}_k : \underline{\underline{\mathrm{E}}}^e_k \tag{3.4}$$

If the volume fraction of region k is c_k, the average elastic strain in the body is

$$\bar{\underline{\underline{\mathrm{E}}}}^e = \sum_{k=1}^{N} c_k \underline{\underline{\mathrm{E}}}^e_k \tag{3.5}$$

The average stress is likewise

$$\bar{\underline{\underline{\mathrm{S}}}} = \sum_{k=1}^{N} c_k \underline{\underline{\mathrm{S}}}_k = \sum_{k=1}^{N} c_k \mathbb{C}_k : \underline{\underline{\mathrm{E}}}^e_k \tag{3.6}$$

Concentration tensors $\mathbb{A}_k$ are defined such that

$$\underline{\underline{\mathrm{E}}}^e_k = \mathbb{A}_k : \bar{\underline{\underline{\mathrm{E}}}}^e \tag{3.7}$$

Combining (3.6) and (3.7),

$$\bar{\underline{\underline{\mathrm{S}}}} = \sum_{k=1}^{N} c_k \bar{\underline{\underline{\mathrm{S}}}}_k = \left(\sum_{k=1}^{N} c_k \mathbb{C}_k : \mathbb{A}_k \right) : \bar{\underline{\underline{\mathrm{E}}}}^e \tag{3.8}$$

Following (3.8), the effective elastic tensor is defined as

$$\mathbb{C}_{\mathrm{eff}} = \sum_{k=1}^{N} c_k \mathbb{C}_k : \mathbb{A}_k \tag{3.9}$$

so that

$$\bar{\underline{\underline{\mathrm{S}}}} = \mathbb{C}_{\mathrm{eff}} : \bar{\underline{\underline{\mathrm{E}}}}^e \tag{3.10}$$

From the case where the material properties are uniform, a constraint emerges:

$$\mathbb{I} = \sum_{k=1}^{N} c_k \mathbb{A}_k \tag{3.11}$$

Now, assuming that $\underline{\underline{\mathrm{E}}}^e_k \equiv \bar{\underline{\underline{\mathrm{E}}}}^e$, gives $\mathbb{A}_k \equiv \mathbb{I}$, and

$$\mathbb{C}^{isostrain}_{\mathrm{eff}} = \sum_{k=1}^{N} c_k \mathbb{C}_k \tag{3.12}$$

On the other hand, if assuming that $\underline{\underline{\mathrm{S}}}_k \equiv \bar{\underline{\underline{\mathrm{S}}}}$, similar logic as above yields

$$\mathbb{C}^{isostress}_{\mathrm{eff}} = \left(\sum_{k=1}^{N} c_k \mathbb{C}_k^{-1} \right)^{-1} \tag{3.13}$$

An simple but effective approximation, based on the observation in [4] that $\mathbb{C}_{\text{eff}}^{isostress} \leq \mathbb{C}_{\text{eff}} \leq \mathbb{C}_{\text{eff}}^{isostrain}$, is an average of the two bounds:

$$\mathbb{C}_{\text{eff}}^{bounds-mean} = \frac{1}{2}\left(\mathbb{C}_{\text{eff}}^{isostress} + \mathbb{C}_{\text{eff}}^{isostrain}\right) \tag{3.14}$$

A class of approximations based on Equation (3.9) uses the notion of a homogeneous reference medium with elastic tensor $\mathbb{C}_{\text{ref}}$, and assumes the equivalence

$$\mathbb{C}_k : \left(\bar{\underline{\underline{\mathrm{E}}}}^e + \tilde{\underline{\underline{\mathrm{E}}}}_k^e\right) = \mathbb{C}_{\text{ref}} : \left(\bar{\underline{\underline{\mathrm{E}}}}^e + \tilde{\underline{\underline{\mathrm{E}}}}_k^e - \underline{\underline{\Lambda}}_k\right) \tag{3.15}$$

where $\tilde{\underline{\underline{\mathrm{E}}}}_k^e$ is the difference between the average elastic strain and the elastic strain in constituent k, and $\underline{\underline{\Lambda}}_k$ is an eigenstrain tensor that represents the mismatch between the elastic properties of constituent k and the reference medium. The Eshelby [5] tensor $\mathbb{S}_k$ is defined such that

$$\tilde{\underline{\underline{\mathrm{E}}}}_k^e = \mathbb{S}_k : \underline{\underline{\Lambda}}_k \tag{3.16}$$

From (3.15) and (3.16),

$$\bar{\underline{\underline{\mathrm{E}}}}^e = \left[\left(\mathbb{C}_{\text{ref}}^{-1} : \mathbb{C}_k - \mathbb{I}\right)^{-1} - \mathbb{S}_k\right] : \underline{\underline{\Lambda}}_k \tag{3.17}$$

The interaction tensor $\mathbb{T}_k$ is defined so that

$$\underline{\underline{\mathrm{E}}}_k^e = \bar{\underline{\underline{\mathrm{E}}}}^e + \tilde{\underline{\underline{\mathrm{E}}}}_k^e = \mathbb{T}_k : \underline{\underline{\mathrm{E}}}_{\text{ref}}^e \tag{3.18}$$

Then from (3.17) and (3.18),

$$\mathbb{T}_k = \left[\mathbb{I} + \mathbb{S}_k : \mathbb{C}_{\text{ref}}^{-1} : \left(\mathbb{C}_k - \mathbb{C}_{\text{ref}}\right)\right]^{-1} \tag{3.19}$$

A class of approximations use the Eshelby tensor $\mathbb{S}$ to derive a concentration tensor $\mathbb{A}$ that produces an effective elasticity tensor. The dilute approximation assumes that each phase is an isolated inhomogeneity, so that the reference strain is approximately equal to the average strain in the body $\bar{\underline{\underline{\mathrm{E}}}}^e$. Then, comparing Equations (3.7) and (3.18),

$$\mathbb{A}_k^{\text{dilute}} = \mathbb{T}_k \tag{3.20}$$

The *Mori-Tanaka* approximation assumes that the reference strain is approximately equal to the (uniform) strain $\underline{\underline{\mathrm{E}}}_0^e$ in the *matrix* phase ($k = 0$), so that

$$\underline{\underline{\mathrm{E}}}_k^e = \mathbb{T}_k : \underline{\underline{\mathrm{E}}}_0^e \tag{3.21}$$

Then

$$\bar{\underline{\underline{\mathrm{E}}}}^e = \sum_{k=1}^{N} c_k \underline{\underline{\mathrm{E}}}_k^e = \sum_{k=1}^{N} c_k \mathbb{T}_k : \underline{\underline{\mathrm{E}}}_0^e \tag{3.22}$$

Combining (3.21) and (3.22),

$$\underline{\underline{\mathbb{E}}}_k^e = \mathbb{T}_k : \left(\sum_{k=1}^{N} c_k \mathbb{T}_k \right)^{-1} : \bar{\underline{\underline{\mathbb{E}}}}^e \tag{3.23}$$

That is,

$$\mathbb{A}_k^{\mathrm{mt}} = \mathbb{T}_k : \left(\sum_{k=1}^{N} c_k \mathbb{T}_k \right)^{-1} \tag{3.24}$$

The *self-consistent* approximation assumes

$$\mathbb{C}_{\mathrm{ref}} = \mathbb{C}_{\mathrm{eff}} \tag{3.25}$$

$$\underline{\underline{\mathbb{E}}}_{\mathrm{ref}}^e = \bar{\underline{\underline{\mathbb{E}}}}^e \tag{3.26}$$

so that

$$\mathbb{A}_k^{\mathrm{sc}} = \left[\mathbb{I} + \bar{\mathbb{S}}_k : \left(\mathbb{C}_{\mathrm{eff}}^{-1} : \mathbb{C}_k - \mathbb{I} \right) \right]^{-1} \tag{3.27}$$

where $\bar{\mathbb{S}}_k$ is constructed using $\mathbb{C}_{\mathrm{eff}}$. These methods are applied to analyze the effective elastic behavior of polycrystalline aggregates in the following sections.

3.1.2. Anisotropy

For an anisotropic material, the apparent properties of the material are dependent on the orientation of the material. For example, the elastic behavior is often represented by a linear elastic relationship embodied by an elastic tensor $\mathbb{C}$. This elastic tensor has a canonical form deriving from the symmetry of the material, typically specified by a set of components and a tensor basis. The orientation of the material specifies a relationship between the material basis, which is constructed with reference to preferred directions within the material, and the spatial basis, which is commonly taken as a Cartesian frame of reference in a physical setting. A common representation of material orientation is given by the Bunge Euler angle triplet, $\left(\phi_1, \Phi, \phi_2\right)$, which can be used to construct the linear map $\underline{\underline{\mathrm{R}}}$ from the spatial basis to the material basis, as:

$$\underline{\underline{\mathrm{R}}}\left(\phi_1, \Phi, \phi_2\right) = \begin{bmatrix} \cos\phi_1 \cos\phi_2 - \cos\Phi \sin\phi_1 \sin\phi_2 & -\cos\phi_1 \sin\phi_2 - \cos\Phi \cos\phi_2 \sin\phi_1 & \sin\phi_1 \sin\Phi \\ \cos\phi_2 \sin\phi_1 + \cos\phi_1 \cos\Phi \sin\phi_2 & \cos\phi_1 \cos\Phi \cos\phi_2 - \sin\phi_1 \sin\phi_2 & -\cos\phi_1 \sin\Phi \\ \sin\Phi \sin\phi_2 & \cos\phi_2 \sin\Phi & \cos\Phi \end{bmatrix} \tag{3.28}$$

For real materials, with spatially varying orientation, it is often advantageous to compute an approximation $\tilde{\mathbb{C}}$, for the effective elastic tensor of the material. One method for producing such an approximation is analyzed in the following.

Given an approximation $\tilde{\mathbb{C}}$, the difference between the actual and approximate elastic strain energies for a given strain $\underline{\underline{\mathbb{E}}}^e$ is

$$\Delta W^e = \underline{\underline{\mathbb{E}}}^e : \mathbb{C} : \underline{\underline{\mathbb{E}}}^e - \underline{\underline{\mathbb{E}}}^e : \tilde{\mathbb{C}} : \underline{\underline{\mathbb{E}}}^e = \underline{\underline{\mathbb{E}}}^e : \left(\mathbb{C} - \tilde{\mathbb{C}} \right) : \underline{\underline{\mathbb{E}}}^e \tag{3.29}$$

The approximation that minimizes the absolute value of the expectation of the difference in elastic strain energy between the true model and the approximate model is,

$$\bar{\mathbb{C}}(\underline{\underline{\mathbb{E}}}^e)=\arg\min_{\tilde{\mathbb{C}}}\left|\int_{\phi_1}\int_{\Phi}\int_{\phi_2} f(\phi_1,\Phi,\phi_2)\underline{\underline{\mathbb{E}}}^e:\left[\mathbb{C}(\phi_1,\Phi,\phi_2)-\tilde{\mathbb{C}}(\phi_1,\Phi,\phi_2)\right]:\underline{\underline{\mathbb{E}}}^e\, d\phi_1 d\Phi d\phi_2\right| \tag{3.30}$$

Here, the Bunge Euler angles $\{\phi_1,\Phi,\phi_2\}$ are used as a convenient parametrization of the orientation space, and $f\left(\phi_1,\Phi,\phi_2\right)$ is the probability density at $\left(\phi_1,\Phi,\phi_2\right)$. This can be generalized by computing the expectation over all strains to obtain a single approximation for $\tilde{\mathbb{C}}$, as in

$$\bar{\mathbb{C}}=\arg\min_{\tilde{\mathbb{C}}}\left|\int_{\underline{\underline{\mathbb{E}}}^e}\int_{\phi_1}\int_{\Phi}\int_{\phi_2} f\left(\underline{\underline{\mathbb{E}}}^e,\phi_1,\Phi,\phi_2\right)\underline{\underline{\mathbb{E}}}^e:\left[\mathbb{C}(\phi_1,\Phi,\phi_2)-\tilde{\mathbb{C}}(\phi_1,\Phi,\phi_2)\right]:\underline{\underline{\mathbb{E}}}^e\, d\underline{\underline{\mathbb{E}}}^e d\phi_1 d\Phi d\phi_2\right| \tag{3.31}$$

Assuming that $\underline{\underline{\mathbb{E}}}^e$ and $\{\phi_1,\Phi,\phi_2\}$ are independent, $f(\underline{\underline{\mathbb{E}}}^e,\phi_1,\Phi,\phi_2)=f(\underline{\underline{\mathbb{E}}}^e)f\left(\phi_1,\Phi,\phi_2\right)$, so that

$$\bar{\mathbb{C}}=\arg\min_{\tilde{\mathbb{C}}}\left|\int_{\underline{\underline{\mathbb{E}}}^e} f(\underline{\underline{\mathbb{E}}}^e)\underline{\underline{\mathbb{E}}}^e:\int_{\phi_1}\int_{\Phi}\int_{\phi_2} f(\phi_1,\Phi,\phi_2)\left[\mathbb{C}(\phi_1,\Phi,\phi_2)-\tilde{\mathbb{C}}(\phi_1,\Phi,\phi_2)\right] d\phi_1 d\Phi d\phi_2 :\underline{\underline{\mathbb{E}}}^e\, d\underline{\underline{\mathbb{E}}}^e\right| \tag{3.32}$$

Commonly, the strain dependence of the approximation is ignored, effectively assuming a uniform distribution, $f(\underline{\underline{\mathbb{E}}}^e)$. In this case,

$$\bar{\mathbb{C}}=\arg\min_{\tilde{\mathbb{C}}}\left|\int_{\phi_1}\int_{\Phi}\int_{\phi_2} f\left(\phi_1,\Phi,\phi_2\right)\left[\mathbb{C}\left(\phi_1,\Phi,\phi_2\right)-\tilde{\mathbb{C}}\left(\phi_1,\Phi,\phi_2\right)\right] d\phi_1 d\Phi d\phi_2\right| \tag{3.33}$$

This approximation can be computed for an arbitrary material; materials with uniformly random orientations approach an isotropic (orientation-independent) approximation in the limit. For such materials, $\tilde{\mathbb{C}}$ is independent of $\left(\phi_1,\Phi,\phi_2\right)$, and

$$\mathbb{C}^{iso}=\bar{\mathbb{C}}=\int_{\phi_1}\int_{\Phi}\int_{\phi_2} f\left(\phi_1,\Phi,\phi_2\right)\mathbb{C}\left(\phi_1,\Phi,\phi_2\right) d\phi_1 d\Phi d\phi_2 \tag{3.34}$$

Rather than evaluate this integral, an equivalent choice of $\mathbb{C}^{iso}$ can be obtained via the following reasoning. First, the space of isotropic fourth-order tensors admits the orthonormal basis,

$$\mathbb{P}^{sph}=\frac{1}{N}\left(\sum_{i=1}^{N}\underline{e}_i\otimes\underline{e}_i\right)\otimes\left(\sum_{i=1}^{N}\underline{e}_i\otimes\underline{e}_i\right) \tag{3.35}$$

$$\mathbb{P}^{symdev}=\sqrt{\frac{2}{N^2+N-2}}\left[\frac{1}{2}\sum_{i=1}^{N}\sum_{j=1}^{N}\left(\underline{e}_i\otimes\underline{e}_j\otimes\underline{e}_i\otimes\underline{e}_j+\underline{e}_i\otimes\underline{e}_j\otimes\underline{e}_j\otimes\underline{e}_i\right)-\mathbb{P}^{sph}\right] \tag{3.36}$$

$$\mathbb{P}^{skew}=\sqrt{\frac{1}{2(N^2-N)}}\sum_{i=1}^{N}\sum_{j=1}^{N}\left(\underline{e}_i\otimes\underline{e}_j\otimes\underline{e}_i\otimes\underline{e}_j-\underline{e}_i\otimes\underline{e}_j\otimes\underline{e}_j\otimes\underline{e}_i\right) \tag{3.37}$$

where N is the number of spatial dimensions. Since elastic tensors $\mathbb{C}$ have minor symmetry (and thus $\mathbb{P}^{skew}::\mathbb{C}=0$), an isotropic elastic tensor can be written as

$$\mathbb{C}=C^{sph}\mathbb{P}^{sph}+C^{symdev}\mathbb{P}^{symdev} \tag{3.38}$$

Define an isotropic elastic tensor via

$$\mathbb{C}^{iso} = \left(\mathbb{P}^{sph} :: \mathbb{C}\right)\mathbb{P}^{sph} + \left(\mathbb{P}^{symdev} :: \mathbb{C}\right)\mathbb{P}^{symdev} \tag{3.39}$$

Now, $\mathbb{C} = \mathbb{C}^{iso} + \mathbb{C}^{*}$, where the isotropic part of $\mathbb{C}^{*}$ is null. Since any anisotropic part of $\mathbb{C}$ is required to vanish for uniformly random orientations,

$$\int_{\phi_1}\int_{\Phi}\int_{\phi_2} f\left(\phi_1,\Phi,\phi_2\right)\mathbb{C}\left(\phi_1,\Phi,\phi_2\right)\, d\phi_1 d\Phi d\phi_2 \tag{3.40}$$

$$= \int_{\phi_1}\int_{\Phi}\int_{\phi_2} f\left(\phi_1,\Phi,\phi_2\right)\left[\mathbb{C}^{iso} + \mathbb{C}^{*}\left(\phi_1,\Phi,\phi_2\right)\right] d\phi_1 d\Phi d\phi_2 \tag{3.41}$$

$$= C^{sph}\mathbb{P}^{sph} + C^{symdev}\mathbb{P}^{symdev} + \int_{\phi_1}\int_{\Phi}\int_{\phi_2} f\left(\phi_1,\Phi,\phi_2\right)\mathbb{C}^{*}\left(\phi_1,\Phi,\phi_2\right) d\phi_1 d\Phi d\phi_2 \tag{3.42}$$

$$= C^{sph}\mathbb{P}^{sph} + C^{symdev}\mathbb{P}^{symdev} \tag{3.43}$$

Thus, the tensor defined in (3.39) is equivalent to that defined in (3.34) for uniformly random orientations.

3.1.3. Cubic materials

As an example, consider materials with cubic symmetry in three dimensions. For these materials, the elastic tensor admits the following compact representation:

$$\mathbb{C}^{cubic} = C_{11}\mathbb{E}^{(11)} + C_{12}\mathbb{E}^{(12)} + C_{44}\mathbb{E}^{(44)} \tag{3.44}$$

where C_{11}, C_{12}, and C_{44} are material constants, and the orthogonal tensor basis is given by:

$$\mathbb{E}^{(11)} = \sum_{i=1}^{3} \underline{e}_i \otimes \underline{e}_i \otimes \underline{e}_i \otimes \underline{e}_i \tag{3.45}$$

$$\mathbb{E}^{(12)} = \sum_{i=1}^{3}\sum_{j=1}^{3} \underline{e}_i \otimes \underline{e}_i \otimes \underline{e}_j \otimes \underline{e}_j - \mathbb{E}^{(11)} \tag{3.46}$$

$$\mathbb{E}^{(44)} = \sum_{i=1}^{3}\sum_{j=1}^{3} \underline{e}_i \otimes \underline{e}_j \otimes \underline{e}_i \otimes \underline{e}_j + \underline{e}_i \otimes \underline{e}_j \otimes \underline{e}_j \otimes \underline{e}_i - 2\mathbb{E}^{(11)} \tag{3.47}$$

with $\underline{e}_i$ representing the i-th cube axis in the material. This representation brings out the fundamental dependence of the material behavior on the constants C_{11}, C_{12}, and C_{44}. The isotropic part of $\mathbb{C}^{cubic}$ is

$$\mathbb{C}^{iso} = \left(\mathbb{P}^{sph} :: \mathbb{C}^{cubic}\right)\mathbb{P}^{sph} + \left(\mathbb{P}^{symdev} :: \mathbb{C}^{cubic}\right)\mathbb{P}^{symdev} \tag{3.48}$$

$$= \left(C_{11} + 2C_{12}\right)\mathbb{P}^{sph} + \frac{2}{\sqrt{5}}\left(C_{11} - C_{12} + 3C_{44}\right)\mathbb{P}^{symdev} \tag{3.49}$$

$$= C_{11}\left(\mathbb{P}^{sph} + \frac{2}{\sqrt{5}}\mathbb{P}^{symdev}\right) + C_{12}\left(2\mathbb{P}^{sph} - \frac{2}{\sqrt{5}}\mathbb{P}^{symdev}\right) + C_{44}\left(\frac{6}{\sqrt{5}}\mathbb{P}^{symdev}\right) \tag{3.50}$$

That is,

$$\mathbb{C}^{iso} = C'_{11}\mathbb{E}^{(11)} + C'_{12}\mathbb{E}^{(12)} + C'_{44}\mathbb{E}^{(44)} \tag{3.51}$$

with

$$\begin{aligned} C'_{11} &= \frac{1}{5}\left(3C_{11} + 2C_{12} + 4C_{44}\right) \\ C'_{12} &= \frac{1}{5}\left(C_{11} + 4C_{12} - 2C_{44}\right) \\ C'_{44} &= \frac{1}{5}\left(C_{11} - C_{12} + 3C_{44}\right) \end{aligned} \tag{3.52}$$

It can be easily verified that $\left\{C'_{11}, C'_{12}, C'_{44}\right\}$ satisfy the requirement of isotropy for an arbitrary cubic material given by

$$C_{44} = \frac{1}{2}\left(C_{11} - C_{12}\right) \tag{3.53}$$

By construction, the expectation of ΔW^e (Equation (3.29)) is 0, but an open question is how to measure the fitness of this optimal approximation. Again, the difference in strain energy is

$$\Delta W^e = E^e_{ij}E^e_{kl}\left(C'_{ijkl} - C^{iso}_{ijkl}\right) = E^{e'}_{mn}E^{e'}_{pq}\left(C_{mnpq} - C^{iso}_{mnpq}\right) \tag{3.54}$$

with

$$E^{e'}_{mn} = E^e_{ij}R_{im}R_{jn} \tag{3.55}$$

The difference between the cubic and isotropic tensors is

$$\begin{aligned} \mathbb{C} - \mathbb{C}^{iso} &= C_\Delta\left(\mathbb{E}^{(11)} - \frac{1}{2}\mathbb{E}^{(12)} - \frac{1}{2}\mathbb{E}^{(44)}\right) \\ C_\Delta &= \frac{2}{5}\left(C_{11} - C_{12} - 2C_{44}\right) \end{aligned} \tag{3.56}$$

Inserting (3.56) into (3.54),

$$\begin{aligned} \Delta W^e &= C_\Delta E^{e'}_{ij}E^{e'}_{kl}\left(\mathbb{E}^{(11)} - \frac{1}{2}\mathbb{E}^{(12)} - \frac{1}{2}\mathbb{E}^{(44)}\right) \\ &= C_\Delta\left[\frac{5}{2}\sum_{i=1}^{3}\left(E^{e'}_{ii}\right)^2 - \frac{1}{2}\mathrm{tr}(\underline{\underline{\mathbb{E}}}^{e'})^2 - \underline{\underline{\mathbb{E}}}^{e'} : \underline{\underline{\mathbb{E}}}^{e'}\right] \\ &= C_\Delta\left[\frac{5}{2}\sum_{i=1}^{3}\left(E^{e'}_{ii}\right)^2 - \frac{1}{2}\mathrm{tr}(\underline{\underline{\mathbb{E}}}^{e})^2 - \underline{\underline{\mathbb{E}}}^{e} : \underline{\underline{\mathbb{E}}}^{e}\right] \end{aligned} \tag{3.57}$$

Thus, the difference in elastic strain energy depends on the elastic constants through C_Δ, the orientation of the material through $\frac{5}{2}\sum_{i=1}^{3}\left(E^{e'}_{ii}\right)^2$, and the invariants of the elastic strain tensor through $\frac{1}{2}\mathrm{tr}(\underline{\underline{\mathbb{E}}}^e)^2 + \underline{\underline{\mathbb{E}}}^e : \underline{\underline{\mathbb{E}}}^e$.

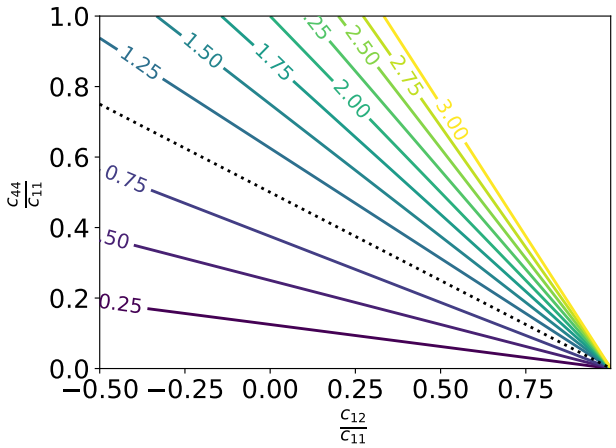

Figure 3-3. The Zener anisotropy ratio for a range of cubic elastic constants. The dashed black line, corresponding to $A = 1$ indicates an isotropic material.

3.1.4. A measure of anisotropy

Isotropy of a cubic single crystal requires that

$$C_{44} = \frac{1}{2}\left(C_{11} - C_{12}\right) \tag{3.58}$$

Given this criterion, a natural measure of anisotropy for cubic single crystals is the Zener anisotropy ratio [6],

$$A = \frac{2C_{44}}{C_{11} - C_{12}} \tag{3.59}$$

Large or small values of A are supposed to indicate a significant degree of anisotropy, while $A = 1$ for isotropic materials. This measure, although widely used, has an unfortunate disconnection from the anisotropy of the material, as shown in Figure 3-3. As seen in the figure, in extreme cases, there are materials with large (or small) anisotropy ratios that are (at least intuitively) relatively isotropic. In any case, the lines of constant A are not parallel to $A = 1$ in the elastic constant space, indicating that comparisons among values of A for different materials are problematic. The measure of anisotropy developed here does not suffer this pathology, as shown in the following.

A natural choice for a measure of anisotropy is

$$\alpha = \frac{\|\mathbb{C} - \mathbb{C}_{iso}\|}{\|\mathbb{C}\|} \tag{3.60}$$

so that

$$0 \leq \alpha \leq 1 \tag{3.61}$$

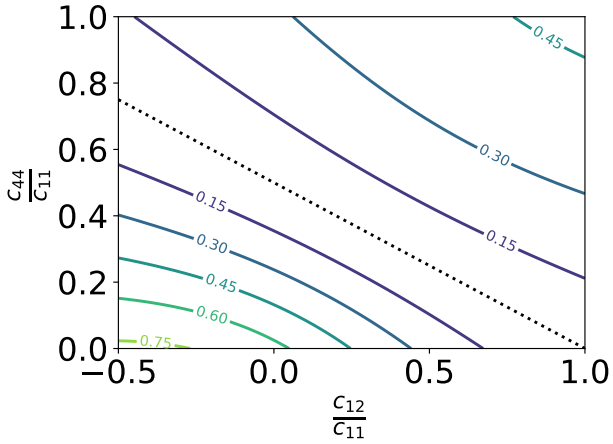

Figure 3-4. The anisotropy measure α for a range of cubic elastic constants.

Given Equation (3.57), for cubic materials,

$$\alpha = \frac{|C_\Delta|}{\|\mathbb{C}\|} = \sqrt{\frac{2}{5}} \frac{\left|1 - \frac{C_{12}}{C_{11}} - 2\frac{C_{44}}{C_{11}}\right|}{\sqrt{1 + 2\left(\frac{C_{12}}{C_{11}}\right)^2 + 4\left(\frac{C_{44}}{C_{11}}\right)^2}} \tag{3.62}$$

For this measure, the anisotropy is plotted as a function of elastic constant ratios in Figure 3-4. In the figure, it is seen that lines of constant α are much closer to parallel to the $\alpha = 0$ line. Furthermore, α provides a quantitative basis for comparing the anisotropy of two materials of different elastic constants: anisotropy is defined as a measure of Euclidean distance between the anisotropic and isotropic elastic tensors, which is directly related to the error in approximating the elastic strain energy for the real material and its isotropic approximation. In addition, it is shown that α has a natural extension for materials without cubic symmetry. Given these intuitively reasonable and mathematically relevant features, the measure α is adopted in the following analysis of elastic anisotropy.

Stability of the crystal lattice requires [7]:

$$-\frac{1}{2} < \frac{C_{12}}{C_{11}} < 1 \tag{3.63}$$

$$0 < \frac{C_{44}}{C_{11}} \tag{3.64}$$

Combining Equations (3.60), (3.63), (3.64),

$$0 \leq \alpha < \sqrt{3/5} \tag{3.65}$$

That is $\alpha = 0$ for isotropic materials, $\alpha \to \sqrt{3/5}$ for $\left(\frac{C_{12}}{C_{11}}, \frac{C_{44}}{C_{11}}\right) \to \left(-\frac{1}{2}, 0\right)$, and $\alpha \to \sqrt{2/5}$ for $\frac{C_{44}}{C_{11}} \to \infty$.

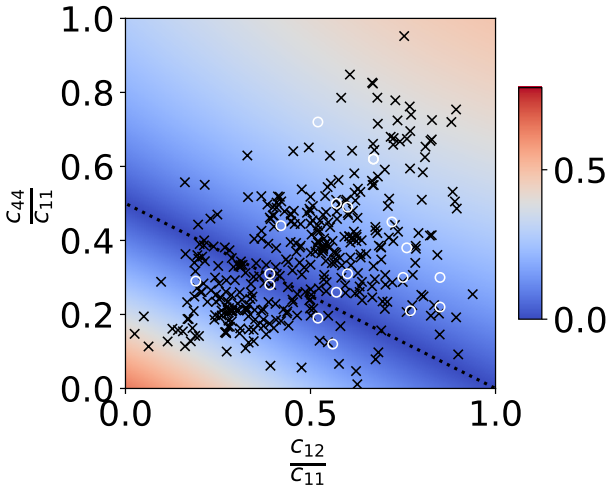

Figure 3-5. Anisotropy of various cubic materials. Data from DFT simulations in [8] (x's) and ultrasonic experiments in [9]–[20] (o's).

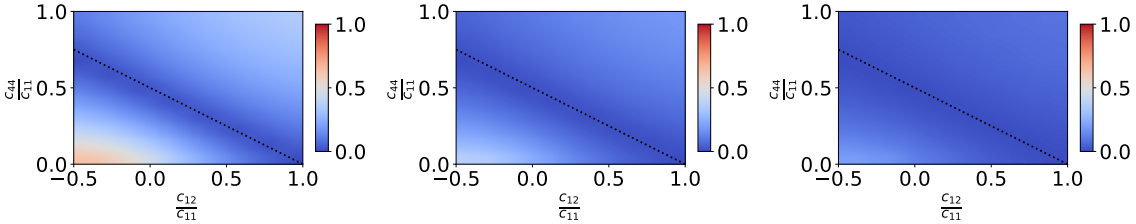

Figure 3-6. Averaged anisotropy, α of polycrystalline aggregates of cubic materials with 2 grains (left), 8 grains (center), and 32 grains (right).

Practically, real cubic materials roughly obey

$$0 < \frac{C_{12}}{C_{11}} < 1 \tag{3.66}$$

$$0 < \frac{C_{44}}{C_{11}} < 1 \tag{3.67}$$

as seen in Figure 3-5.

For polycrystalline materials, there is no guarantee of cubic symmetry, even when the constituent grains possess cubic symmetry. The scaling of α with respect to the number of grains in a polycrystalline aggregate illuminates the effects of single crystal anisotropy on polycrystalline anisotropy. The contours of α for aggregates with 2, 8, and 32 grains are shown in Figure 3-6. The scaling of the anisotropy is well-captured with a simple power law:

$$\alpha = \alpha_0 - c_\alpha L^{\frac{3}{2}} d_g^{-\frac{3}{2}} \tag{3.68}$$

where L is the size of the aggregate, and d_g is the average size of the constituents. The scaling for austenite is shown in Figure 3-7.

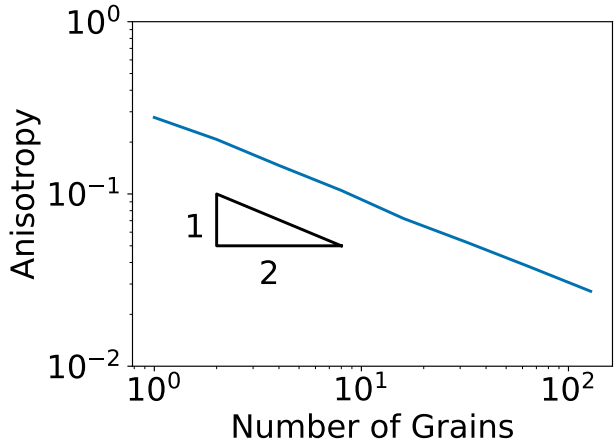

Figure 3-7. Effective anisotropy of polycrystalline austenite as a function of number of grains.

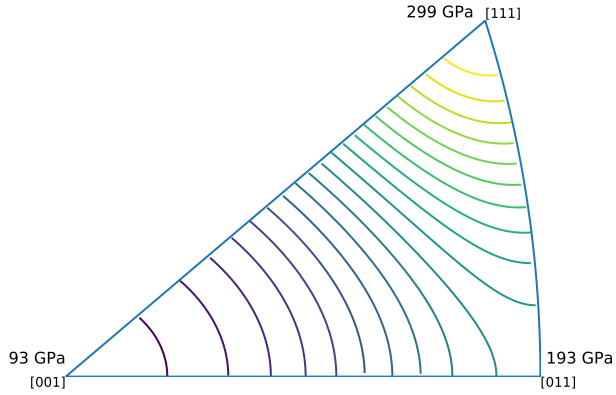

Figure 3-8. The effective Young's modulus for a single crystal of austenitic stainless steel as a function of crystal orientation.

3.1.5. Effective Young's Modulus

One upshot of elastic anisotropy is that the effective Young's modulus of the material depends on the orientation of the loading with respect to the material basis. As shown in Figure 3-8, the modulus of an austenitic stainless steel crystal varies widely depending on the orientation. For polycrystalline aggregates, the effective Young's modulus varies according to the constituent orientations and morphology. Using the idealized morphologies shown in Figure 3-9, this effect is now analyzed. Keeping the morphology fixed, orientations are drawn from a uniform distribution and assigned to the constituent grains. The predicted Young's moduli for a number of realizations are shown in Figure 3-10. A number of features are evident in the figure. First, the isostrain approximation produces an upper-bound prediction of modulus, while the isostress approximation produces a lower-bound prediction. The average of these two predictions is an effective prediction, and only slightly outperformed by the self-consistent method. Second, the average has a weak dependence on the number of grains, increasing slightly with increasing numbers of grains up to an asymptotic limit. The results are summarized in Figure 3-11. Last, the spread in predicted (and observed) moduli is higher for the 8 grain morphology, as expected. This effect

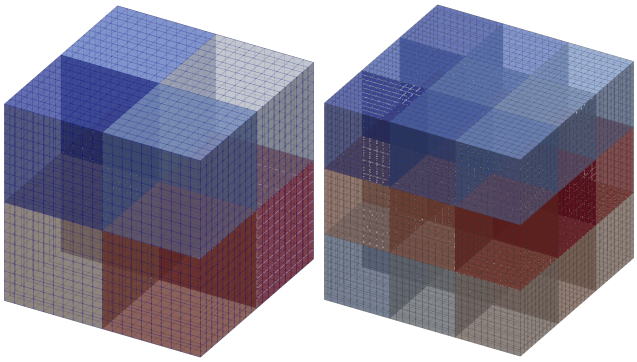

Figure 3-9. Idealized polycrystalline aggregates.

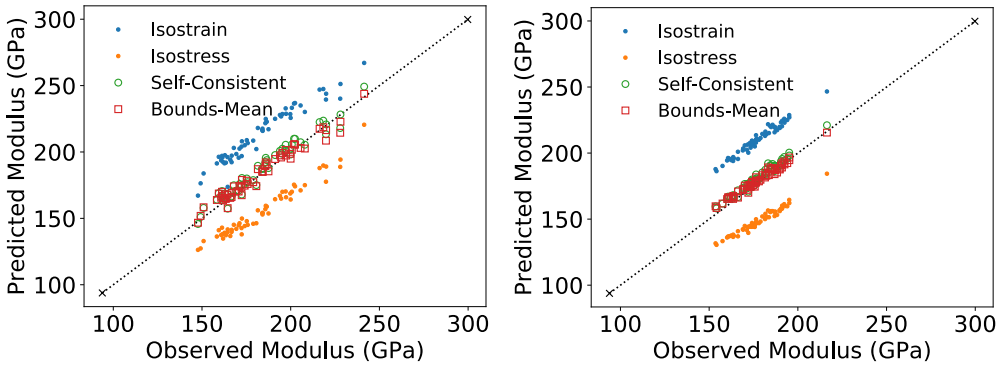

Figure 3-10. Predicted effective Young's moduli for 8 grain microstructures (left) and 27 grain microstructures (right).

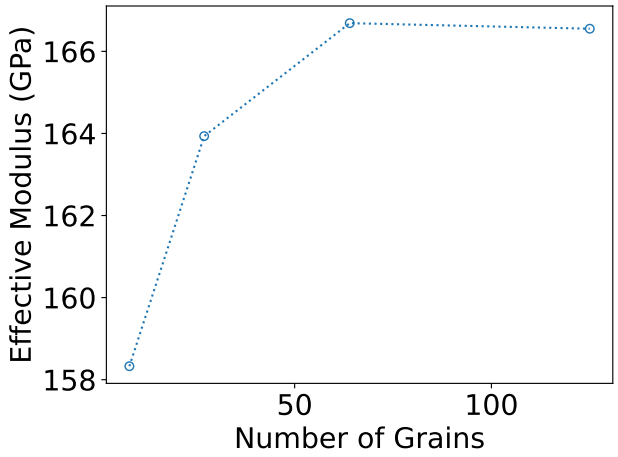

Figure 3-11. Average effective modulus as a function of morphology size.

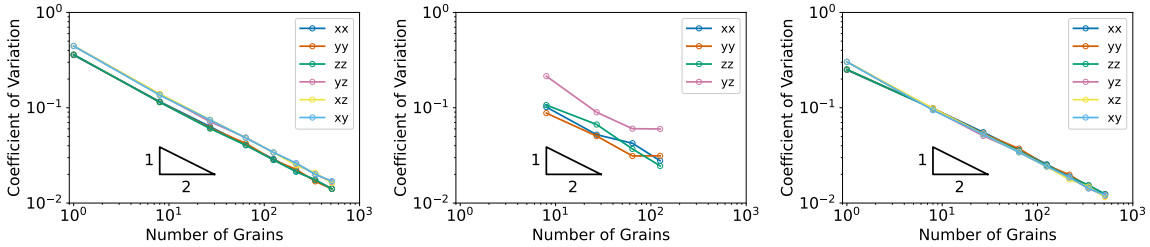

Figure 3-12. Coefficients of variation of elastic moduli as a function of morphology size, computed via the isostress approximation (left), DNS (center), and the isostrain approximation (right).

was quantified for a range of morphology sizes, and the results are summarized in Figure 3-12. In the figure, it is evident that the coefficients of variation for the apparent moduli scale with the inverse square root of the number of grains in the microstructure. The scaling is well-captured with a simple power law:

$$c_{v,\alpha\beta} = c_{v,\alpha\beta}^{single} - m_{\alpha\beta} L^{\frac{3}{2}} d_g^{-\frac{3}{2}} \tag{3.69}$$

Setting the threshold for significance at a coefficient of variation of 1%, microstructures with on the order of 10^3 or fewer grains show significant variability. For a material with grain sizes on the order of 10μm, this corresponds to a spatial length scale on the order of 100μm.

3.2. Homogenized Plasticity

For plasticity, the homogenization can be treated in a straightforward but computationally demanding way: simulations of polycrystalline aggregates can be used as data to perform model selection and calibration for a suitably inexpensive model. Numerous successful applications of this approach can be found in the literature, but they suffer from the severe limitation that any change in material properties necessitates a new set of expensive simulations for recalibration. Advances in surrogate modeling and other machine learning techniques promise to reduce this marginal cost, but a cheap, interpretable formulation is still required to rapidly turn data into performance predictions or study the sensitivity of outputs to changes in microstructure. One such formulation is detailed and explored in the following sections.

3.2.1. Definition of plastic yielding

The phenomenon of plastic yielding is somewhat hard to define. It is tempting to say that when a material under load experiences any irreversible deformation, that material is yielding. However, all materials undergo entropically-driven changes at finite temperature, and it is very difficult to draw an atomically-sharp line between regimes of reversible and irreversible change. The simplest models of plasticity do this by defining a scalar yield strength, Y, such that a scalar measure of *equivalent* stress, σ^{eqv}, indicates plastic yielding when the stress level reaches the yield strength,

as in

$$\sigma^{\text{eqv}} = Y \tag{3.70}$$

Some widely used criteria of this form are given in Appendix A. The behavior of real materials does not conform to this simple model in a number of important ways. Here, we examine two sources of such deviation: the rate-dependence and the orientation-dependence of plastic yielding. In Appendix B, we consider alternative formulations that might address these issues. For the analysis here, we adopt a criterion based on the fraction, ϕ_{cr}, of the applied power, $\dot{W}$, that is being dissipated by plasticity, $\mathcal{D}$, and define the onset of plastic yielding as satisfaction of the criterion

$$\mathcal{D}^p = \phi_{cr}\dot{W} \tag{3.71}$$

The choice of $\phi_{cr} \in (0, 1]$ is somewhat arbitrary; for rate-dependent plasticity or heterogeneous materials, the choice impacts the shape of the yield locus. The scaling results derived below are relatively insensitive to the choice of ϕ_{cr}, but some of the effects are noted in the analysis that follows. As we show, adopting this criterion allows us to generalize the classical Schmid factor to account for orientation-dependence and rate-dependence in plastic yielding in a thermodynamically consistent fashion.

3.2.2. Generalized Schmid Factor

The generalized Schmid factor (GSF), detailed below, is a quantity that represents the orientation dependence of plastic flow in a general polycrystalline material with well-defined slip systems. The GSF extends the classical Schmid factor to account for rate-dependent plasticity, and predicts the mean and variance in plastic yield, as defined by Equation (3.71) reasonably well across a range of grain morphologies and material rate sensitivity.

The plastic dissipation d^p at a point is given as the sum of the slip-system-wise products of the resolved shear stresses τ^α and the plastic slip rates $\dot{\gamma}^\alpha$:

$$d^p = \sum_{\alpha=1}^{12} \tau^\alpha \dot{\gamma}^\alpha(\tau^\alpha) \tag{3.72}$$

The volume averaged plastic dissipation of the body Ω is

$$\begin{aligned} \mathcal{D}^p &= \frac{1}{|\Omega|}\int_\Omega d^p\left(\underline{x}\right) dV \\ &= \frac{1}{|\Omega|}\sum_{i=1}^{N_{grains}}\int_{\Omega_i} d^p\left(\underline{x}\right) dV \end{aligned} \tag{3.73}$$

Making the simplifying assumption that the plastic dissipation does not vary spatially within a grain,

$$\mathcal{D}^p = \sum_{i=1}^{N_{grains}} \frac{|\Omega_i|}{|\Omega|} d_i^p \tag{3.74}$$

with the help of (3.72). The yield criterion is then based on the fraction ϕ_{cr} of the available applied power being dissipated,

$$\mathcal{D}^p = \phi_{cr} \underline{\underline{\Sigma}} : \underline{\underline{L}} \tag{3.75}$$

where $\underline{\underline{\Sigma}}$ is a representative volume averaged stress, and $\underline{\underline{L}}$ is the averaged velocity gradient.

The representative volume averaged stress and velocity gradient are approximated from the volume average of the applied power density:

$$\dot{W} = \frac{1}{|\Omega|} \int_\Omega \underline{\underline{\sigma}} : \underline{\underline{l}} \, dV \approx \frac{1}{|\Omega|} \left(\int_\Omega \underline{\underline{\sigma}} \, dV \right) : \frac{1}{|\Omega|} \left(\int_\Omega \underline{\underline{l}} \, dV \right) = \underline{\underline{\Sigma}} : \underline{\underline{L}} \tag{3.76}$$

For the problems considered here, which satisfy the Hill-Mandel condition [21], the equality is exact.

Together with (3.74) and (3.75), the yield criterion is then

$$\sum_{i=1}^{N_{grains}} v_i d_i^p = \phi_{cr} \underline{\underline{\Sigma}} : \underline{\underline{L}} \tag{3.77}$$

with the volume fraction

$$v_i = \frac{|\Omega_i|}{|\Omega|} \tag{3.78}$$

The criterion (3.77) becomes quite useful under various simplifying assumptions, as shown below.

In the first case, the stress in each grain is equal to the macroscopic applied stress, an approximation which goes back to [22]. Define the equivalent stress

$$\tau = \sqrt{\underline{\underline{\tau}} : \underline{\underline{\tau}}} \tag{3.79}$$

And the direction

$$\underline{\underline{n}} = \frac{\underline{\underline{\tau}}}{\sqrt{\underline{\underline{\tau}} : \underline{\underline{\tau}}}} = \frac{1}{\tau} \underline{\underline{\tau}} \tag{3.80}$$

Then the Schmid factor is

$$f^\alpha = \frac{\tau^\alpha}{\sqrt{\underline{\underline{\tau}} : \underline{\underline{\tau}}}} = \frac{\tau^\alpha}{\tau} = \underline{\underline{n}} : \underline{\underline{P}}^\alpha \tag{3.81}$$

The plastic dissipation at a point is then

$$d^p = \sum_{\alpha=1}^{N_{ss}} f^\alpha \tau \dot{\gamma}^\alpha (f^\alpha \tau) \tag{3.82}$$

where the definition (3.81) has been used in (3.72). Assuming $\tau \equiv \tau_i$ is constant throughout each grain i, (3.82) yields

$$d_i^p = \tau_i \sum_{\alpha=1}^{N_{ss}} f^\alpha \dot{\gamma}^\alpha \left(f^\alpha \tau_i \right) \tag{3.83}$$

and (3.74) becomes

$$\mathcal{D}^p = \sum_{i=1}^{N_{grains}} v_i \tau_i \sum_{\alpha=1}^{N_{ss}} f^\alpha \dot{\gamma}^\alpha \left(f^\alpha \tau_i \right) \tag{3.84}$$

Assuming $\tau_i \equiv T$ is constant throughout the body Ω,

$$\mathcal{D}^p = T \sum_{i=1}^{N_{grains}} v_i \sum_{\alpha=1}^{N_{ss}} f_i^\alpha \dot{\gamma}^\alpha \left(f_i^\alpha T \right) \tag{3.85}$$

Combining with (3.75), the yield criterion becomes:

$$T \sum_{i=1}^{N_{grains}} v_i \sum_{\alpha=1}^{N_{ss}} f_i^\alpha \dot{\gamma}^\alpha \left(f_i^\alpha T \right) = \phi_{cr} \underline{\underline{\Sigma}} : \underline{\underline{\mathrm{L}}} \tag{3.86}$$

Rearranging,

$$T = \frac{\phi_{cr} \underline{\underline{\Sigma}} : \underline{\underline{\mathrm{L}}}}{\sum_{i=1}^{N_{grains}} v_i \sum_{\alpha=1}^{N_{ss}} f_i^\alpha \dot{\gamma}^\alpha \left(f_i^\alpha T \right)} \tag{3.87}$$

In general, (3.87) can be treated with an appropriate nonlinear solver to determine the value of T. Given the power law formulation (2.15) for $\dot{\gamma}^\alpha (\tau^\alpha)$, the functional form is independent of α, and

$$\dot{\gamma}^\alpha = \dot{\gamma}_0 \left| \frac{f^\alpha T}{g^\alpha} \right|^k \mathrm{sign}(f^\alpha) \tag{3.88}$$

Inserting (3.88) into (3.87), and assuming that

$$\underline{\underline{\Sigma}} \approx T \underline{\underline{\mathrm{n}}} \tag{3.89}$$

we have

$$T = \left[\frac{\phi_{cr} \underline{\underline{\mathrm{n}}} : \underline{\underline{\mathrm{L}}}}{\sum_{i=1}^{N_{grains}} v_i \sum_{\alpha=1}^{N_{ss}} \dot{\gamma}_0 \frac{|f_i^\alpha|^{k+1}}{(g_i^\alpha)^k}} \right]^{1/k} = \frac{\tau_{cr}}{\bar{f}} \tag{3.90}$$

with the critical stress

$$\tau_{cr} = g \left[\frac{\phi_{cr} \underline{\underline{\mathrm{n}}} : \underline{\underline{\mathrm{L}}}}{\dot{\gamma}_0} \right]^{1/k} \tag{3.91}$$

and the GSF for the flow rule (3.88),

$$\bar{f} = \left[\sum_{i=1}^{N_{grains}} v_i \sum_{\alpha=1}^{N_{ss}} \dot{\gamma}_0 \left| f_i^\alpha \right|^{k+1} \frac{g}{\left(g_i^\alpha \right)^k} \right]^{1/k} \tag{3.92}$$

where $g > 0$ is an arbitrary scalar stress value. Assuming $g_i^\alpha \equiv g$ is independent of grain and slip system,

$$T = g\left[\frac{\phi_{cr}\underline{\underline{\mathrm{n}}} : \underline{\underline{\mathrm{L}}}}{\sum_{i=1}^{N_{grains}} v_i \sum_{\alpha=1}^{N_{ss}} \dot{\gamma}_0 \left|f_i^\alpha\right|^{k+1}}\right]^{1/k} \tag{3.93}$$

For a single crystal (with $N_{grains} = 1$ and $v_1 = 1$), the formula for the GSF yield strength simplifies to

$$\begin{aligned} \tau_{cr} &= g\left[\frac{\phi_{cr}\underline{\underline{\mathrm{n}}} : \underline{\underline{\mathrm{L}}}}{\dot{\gamma}_0}\right]^{1/k} \\ \bar{f} &= \left[\sum_{\alpha=1}^{N_{ss}} |f^\alpha|^{k+1}\right]^{1/k} \end{aligned} \tag{3.94}$$

There are a number of simplifications that permit straightforward calculation of the yield strength. For example, taking the limit as $k \to \infty$, we recover the classical formulation for rate independent plasticity:

$$T = \frac{g}{\max_\alpha f^\alpha}, \quad \tau_{cr} = g \tag{3.95}$$

Alternatively, if the stress rate $\dot{T}$ is known, we can use the fact that at yield, (3.75) holds, so that

$$\underline{\underline{\Sigma}} : \underline{\underline{\mathrm{L}}} = \underline{\underline{\Sigma}} : \underline{\underline{\mathrm{L}}}^e + \underline{\underline{\Sigma}} : \underline{\underline{\mathrm{L}}}^p \approx \underline{\underline{\Sigma}} : \underline{\underline{\mathrm{L}}}^e + \phi_{cr}\underline{\underline{\Sigma}} : \underline{\underline{\mathrm{L}}} \tag{3.96}$$

and thus

$$\underline{\underline{\mathrm{L}}} = \frac{1}{1-\phi_{cr}}\underline{\underline{\mathrm{L}}}^e \tag{3.97}$$

The elastic part of the rate of deformation is approximately

$$\underline{\underline{\mathrm{D}}}^e \approx \mathbb{C}^{-1} : \underline{\dot{\mathrm{T}}} = \dot{T}\mathbb{C}^{-1} : \underline{\underline{\mathrm{n}}} \tag{3.98}$$

Thus, the critical stress can be approximated as

$$\tau_{cr} = g\left[\frac{\frac{\phi_{cr}}{1-\phi_{cr}}\dot{T}\,\underline{\underline{\mathrm{n}}} : \mathbb{C}^{-1} : \underline{\underline{\mathrm{n}}}}{\dot{\gamma}_0}\right]^{1/k} \tag{3.99}$$

In the case of rate-controlled uniaxial stress, we have that

$$\underline{\underline{\mathrm{n}}} = \underline{e}_i \otimes \underline{e}_i \tag{3.100}$$

so that

$$\underline{\underline{\mathrm{n}}} : \underline{\underline{\mathrm{D}}} = D_{ii} \quad \text{(no summation)} \tag{3.101}$$

and thus,

$$\tau_{cr} = g\left(\frac{\phi_{cr} D_{ii}}{\dot{\gamma}_0}\right)^{\frac{1}{k}} \tag{3.102}$$

3.2.2.1. Verification for Single Crystal Yield Strengths

A series of crystal plasticity simulations were performed to assess yield strengths for single crystals of various orientations. For each orientation, the complete yield locus was computed by applying a combination of symmetry displacement boundary conditions and traction boundary conditions with a linearly-ramped stress magnitude. Following (A.10), the stresses were applied such that

$$\begin{aligned} T_{11} &= T\cos\left(\theta+\frac{\pi}{6}\right) \\ T_{22} &= T\sin(\theta) \\ T_{33} &= -T\cos\left(\theta-\frac{\pi}{6}\right) \end{aligned} \tag{3.103}$$

with $\dot{T} = 600\text{s}^{-1}$. In the limit where $k \to \infty$, the simplification (3.95) is sufficient, in general, the critical stress for these simulations is determined via (3.99).

Single crystal yield loci were generated by varying θ over the interval $[0, 179°]$ by increments of $1°$. The constitutive formulation is tension-compression symmetric, so that angles in the interval $[180°, 359°]$ are equivalent to the calculated angles. The rate exponents k were also varied, and the results for $k \in [2, 5, 10, 20]$ are shown in Figure 3-13. Figure 3-14 shows comparisons of the predicted and simulated yield strengths for $\theta = \frac{\pi}{6}$, using τ_{cr} as computed from the simulations. As seen in the figure, the agreement is quite good, with the small deviations attributable to the non-uniform stress state induced for orientations where the deformation is inhomogeneous due to the symmetry boundary conditions.

3.2.2.2. Polycrystalline results

For polycrystalline aggregates, Equation (3.93) is only approximate, depending critically on the assumption of uniform stress. Figures 3-15, 3-16, and 3-17 show the results of applying Equation (3.93) for various grain morphologies and orientation distributions. In the figures, it is shown that the approximation (3.93) is reasonable, despite a systematic bias toward over-predicting the yield strength, and under-predicting variability due to microstructural differences. The bias in the predictions is related to the violation of the assumption of uniform stress, and is relatively well-behaved. First, it is noted that a simple linear model can be used to correct the bias, as shown in Figure 3-18. In general, the slope of the linear model is a function of the number of grains in the microstructure, as shown in Figure 3-19. This trend could be used to systematically correct the GSF predictions, yielding a more accurate model. The linear model is a relatively good fit, independent of microstructure, as shown in Figure 3-20. Although the goodness of fit decreases with increasing microstructure size, all values are in the range $[0.65, 0.85]$, indicating a relatively good fit across the range of microstructures. Also, larger microstructures exhibit less variability, so that the lower fit quality for those aggregates is less concerning. The variability in the yield strength is summarized in Figure 3-21, where it can be seen that the coefficient of variation has an approximate inverse square root dependence on the number of grains. Furthermore, it is seen that the scaling of the DNS and GSF predictions are comparable, indicating that the GSF

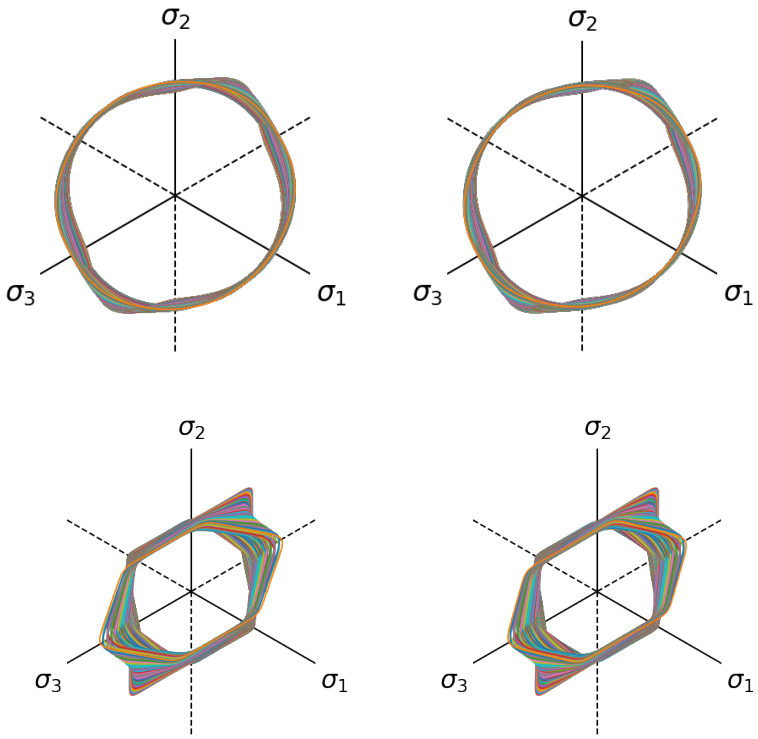

Figure 3-13. Comparison of yield loci for values of the rate exponent $k = 2$ (top row) and $k = 20$ (bottom row) for DNS (left column) and GSF calculations (right column). Note: axes in top and bottom rows are scaled separately to show detail.

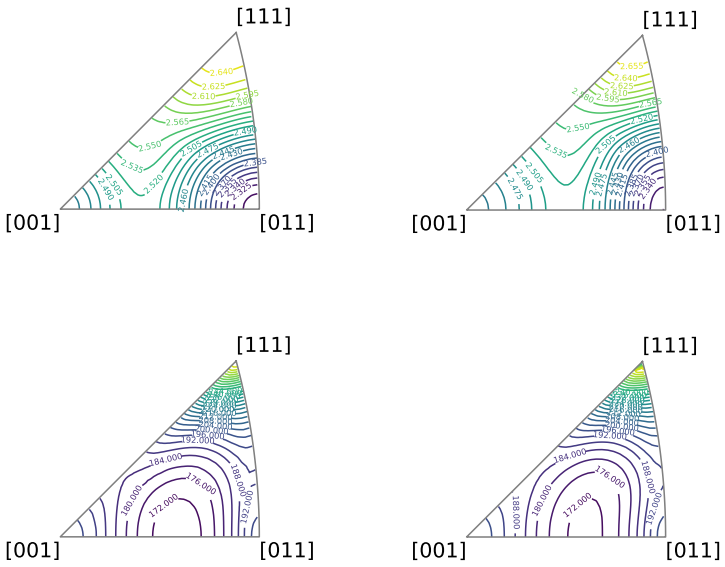

Figure 3-14. Comparison of uniaxial yield strengths for values of the rate exponent $k = 2$ (top row) and $k = 20$ (bottom row) for DNS (left column) and GSF calculations (right column).

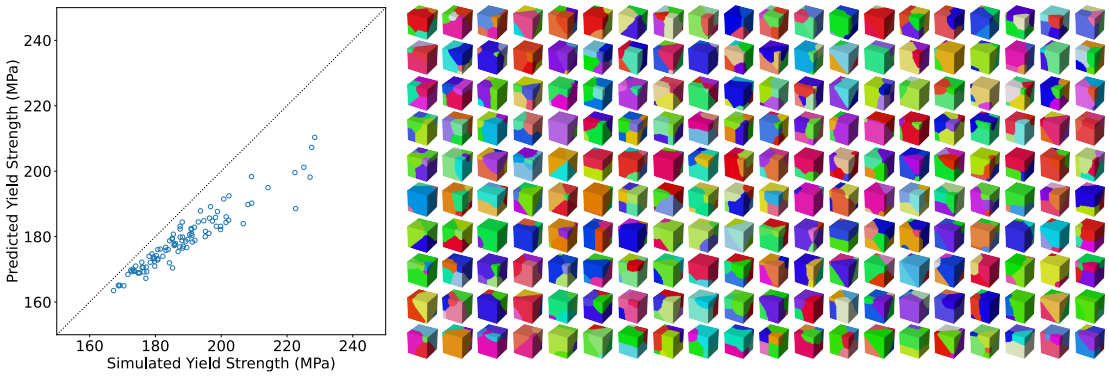

Figure 3-15. Predictions of yield strength via the GSF approximation (left) for an ensemble of polycrystalline aggregates with 5 grains each (right).

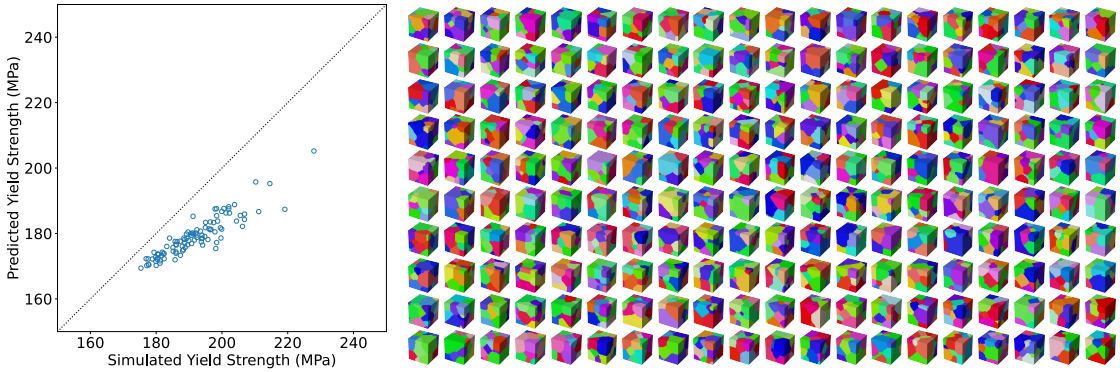

Figure 3-16. Predictions of yield strength via the GSF approximation (left) for an ensemble of polycrystalline aggregates with 10 grains each (right).

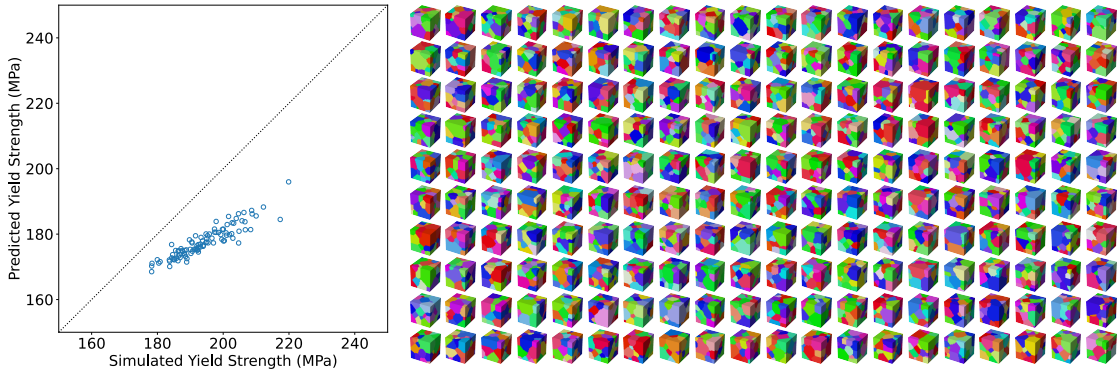

Figure 3-17. Predictions of yield strength via the GSF approximation (left) for an ensemble of polycrystalline aggregates with 20 grains each (right).

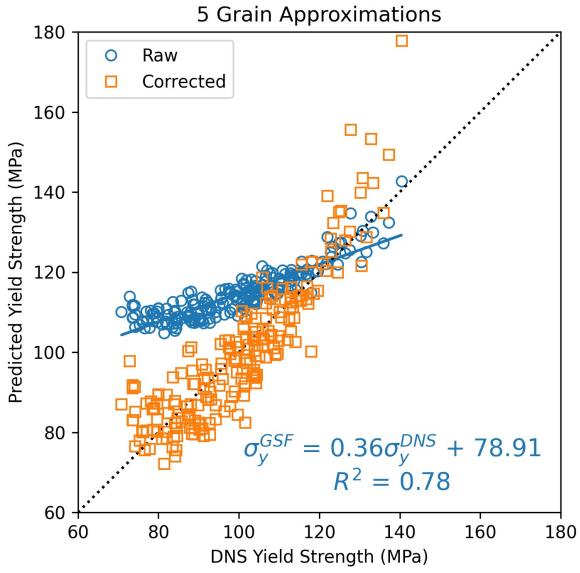

Figure 3-18. Predictions of yield strength via the GSF approximation for an ensemble of polycrystalline aggregates with 5 grains each, both raw and with linear correction applied.

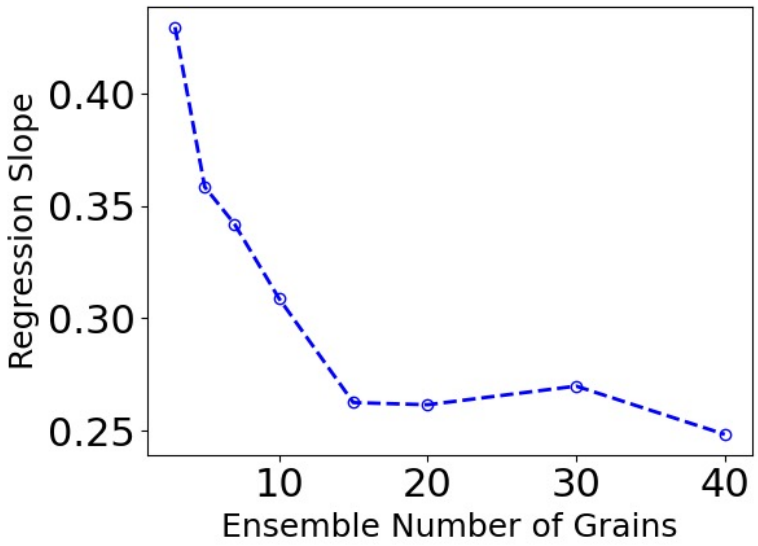

Figure 3-19. Slope of the linear correction as a function of microstructure size.

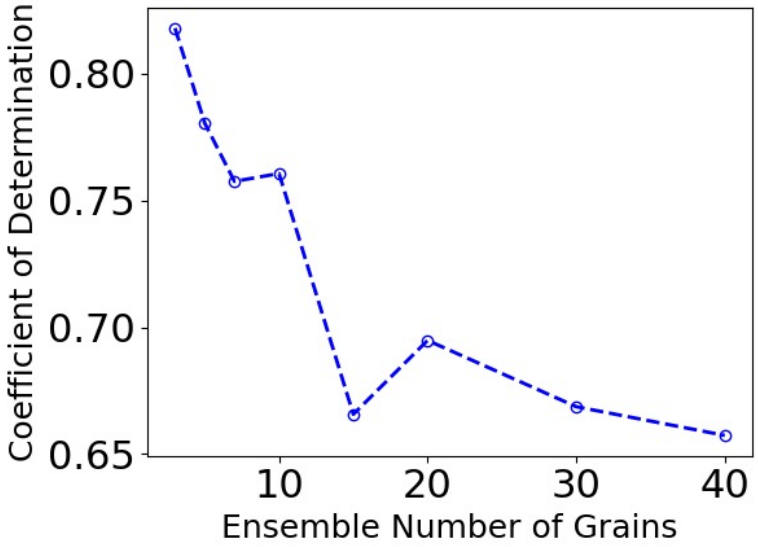

Figure 3-20. Coefficient of determination as a function of microstructure size.

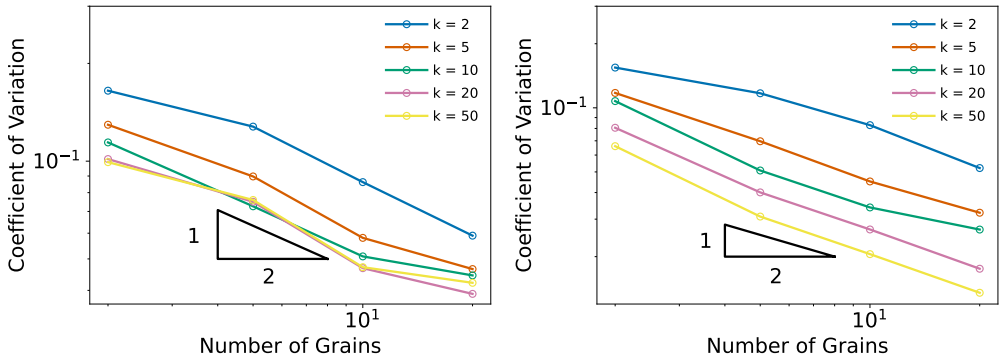

Figure 3-21. Coefficient of variation for yield strength as a function of microstructure size for a range of rate exponents, k; from DNS (left) and GSF approximation (right).

approximation is a useful tool for predicting the effects of length scale on the variability of yield strength.

For the GSF approximation method, another promising result is found for the uncorrected predictions, as shown in Figure 3-22. In the figure, it can be seen that the GSF approximations are relatively good across a range of rate sensitivities and microstructures, and that these predictions for $\phi_{cr} = 0.95$ are conservative, in the sense that the predicted yield strength is always lower than the measured yield strength. Thus, the GSF method provides an effective way to predict yield strength for polycrystalline aggregates.

3.2.3. Yield Surface

To analyze plastic yielding in the microscale simulations performed here, three classical yield models are examined. The Tresca model has a yield surface defined by (A.19). The von Mises model has a yield surface defined by (A.18). The Hosford model has a yield surface defined by (A.20). In the Hosford model, values of $n = 1$ and $n = \infty$ recover the Tresca model, and values of $n = 2$ and $n = 4$ recover the von Mises model. Thus, the Tresca and von Mises models can be thought of as special cases of the Hosford model.

This analysis starts with a maximally-reduced finite element representation (one element per grain) of a highly idealized microstructure with 64 cubic grains arranged in a unit cube. To probe the yield surface of this microstructure, 120 simulations are run under varying principal stress configurations. An example of the stress-state produced is represented in Figure 3-23, where the contour of the first principal stress is plotted.

The microscale model used here is a rate-dependent crystal plasticity model given in Section 2.1. As discussed in Appendix B, it is not straightforward to define plastic yielding for such a model. Here, the criterion (3.77) is adopted where the material is counted as yielding when the plastic power reaches a specified fraction ϕ_{cr} of the total applied power. The results are plotted in Figure 3-24. To analyze these results, the parameters (n, Y) for the Hosford yield surface (A.20) are fit

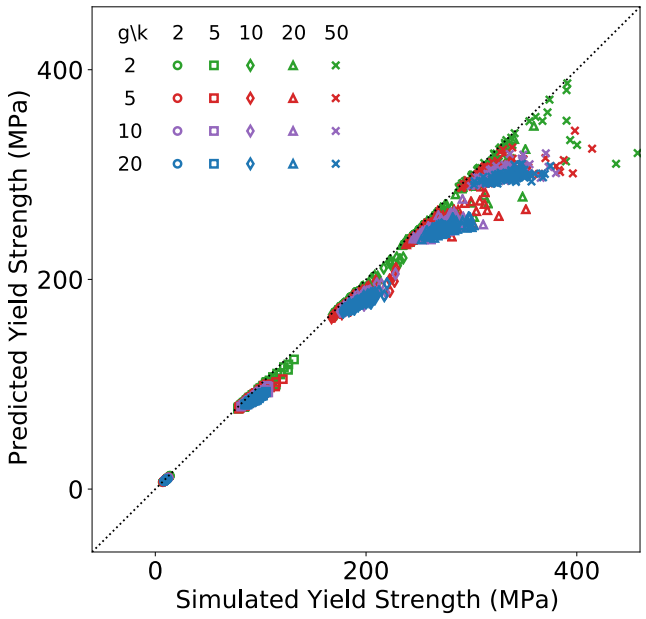

Figure 3-22. Predictions of yield strength via the GSF approximation for ensembles of polycrystalline aggregates with varying numbers grains g and rate exponents k.

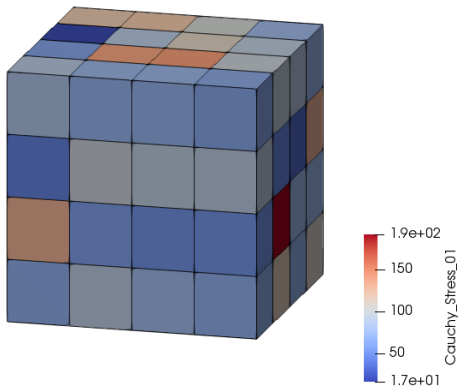

Figure 3-23. Stress contour on simplified microstructure.

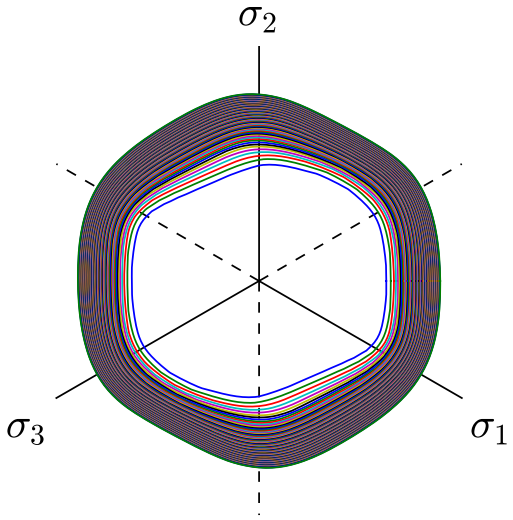

Figure 3-24. Yield loci for specified values $\{0.002, 0.004, \ldots, 0.2\}$ **of** ϕ_{cr}**.**

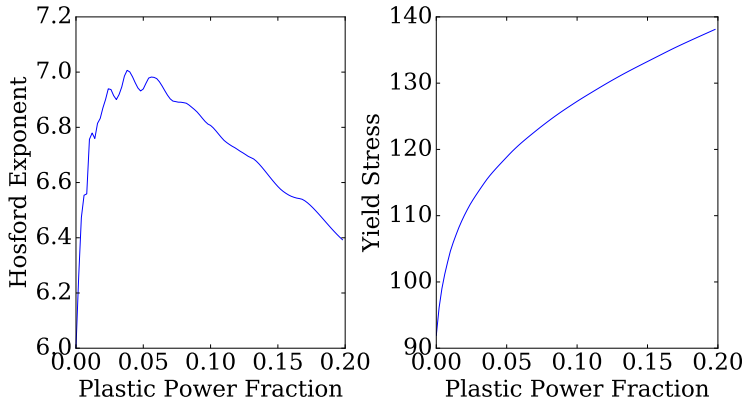

Figure 3-25. Hosford parameters (left, n**; right,** Y**) fit to yield loci for specified values** $\{0.002, 0.004, \ldots, 0.2\}$ **of** ϕ_{cr}**.**

for each computed yield locus. The results are shown in Figure 3-25.

Some simple observations based on Figures 3-24 and 3-25 are made. First, for small values of ϕ_{cr}, the yield locus does not exhibit the six-fold symmetry of the isotropic macroscale models, instead exhibiting only the mathematically required two-fold symmetry. For larger values of ϕ_{cr}, the response approaches the six-fold symmetric character of the macroscale models. Second, the parameter n fit to the microscale data takes on values in the range $[6, 7]$, indicating the aggregated response is somewhere between that of the Tresca and von Mises models. The results of the same analysis applied to a microstructure with 125 cubic grains is shown in Figure 3-26. For this case, it is seen in Figure 3-26 that the lower symmetry behavior is less evident, the yield loci exhibiting the expected six-fold symmetric behavior to a much closer approximation. The parameters fit to the computed yield loci, shown in Figure 3-26 exhibit similar behavior to the 64-grain microstructure, giving some limited confidence that the trends are not artificial. Specifically those

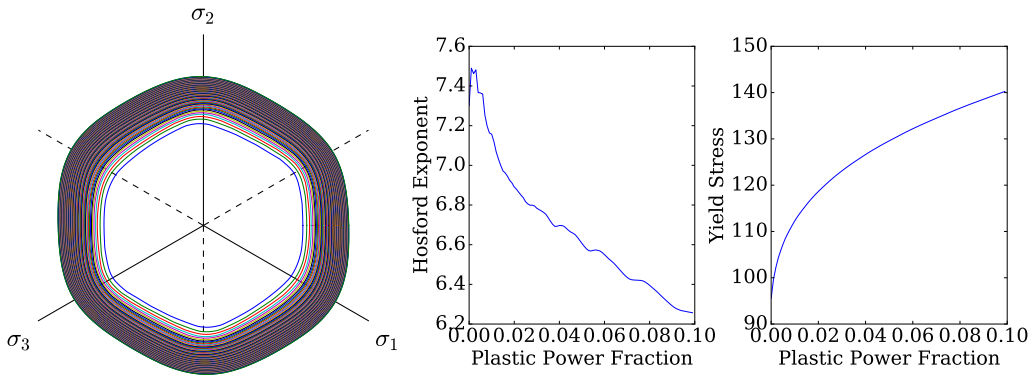

Figure 3-26. Yield behavior for specified values $\{0.002, 0.004, \ldots, 0.2\}$ of ϕ_{cr} for the microstructure with 125 grains: yield loci (left) and best-fit parameter values (n, Y) for the Hosford model (right).

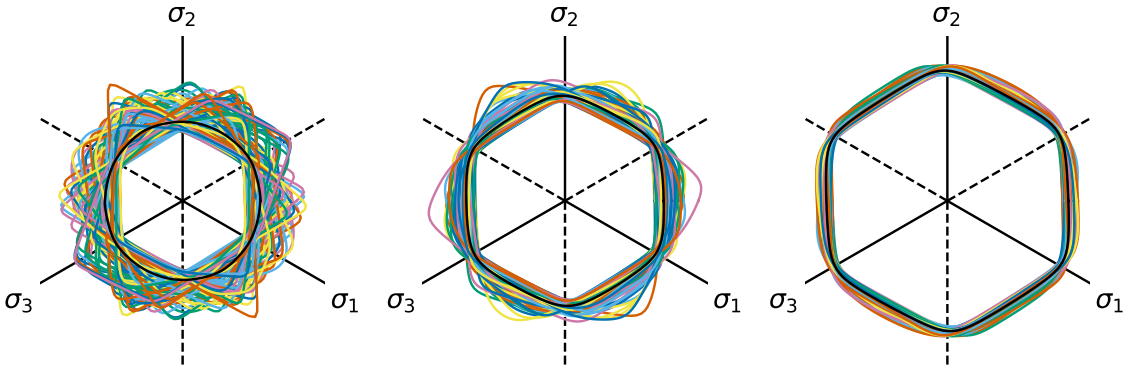

Figure 3-27. Yield loci for 1-grain (left), 4-grain (center), and 16-grain (right) microstructures. The black lines represent the mean responses of the ensembles. Note: axes are scaled separately to show detail.

trends are: 1) the yield locus grows from initial yield with a decreasing rate toward a saturated value; 2) the Hosford exponent decays after a short initial growth, and is in the interval $[6.0, 7.5]$ for all values of ϕ_{cr}.

Using the GSF approximation, yield surfaces are then generated for ensembles of 200 microstructures each for equal volume grain numbers in $[1, 2, 4, 8, 16, 32]$. Results for 1-grain, 4-grain, and 16-grain microstructures are shown in Figure 3-27. In the figure, it can be seen that the yield loci are well-represented by the Hosford yield criterion, and that the variability in yield behavior across an ensemble decreases with increasing numbers of grains. This result is summarized in Figure 3-28. In the left plot, the mean yield strength is plotted as a function of the number of grains, indicating a small decrease in yield strength with increasing grain number. In the right plot, the coefficient of variation in yield strength is plotted as a measure of anisotropy. It is found that the anisotropy decays as the number of grains to the $\frac{3}{4}$ power. The scaling is well-captured with a simple power law:

$$c_v = c_v^{single} - mL^{\frac{9}{4}} d_g^{-\frac{9}{4}} \tag{3.104}$$

It is evident from these results that microstructures must have on the order of 10^2 to 10^3 grains to

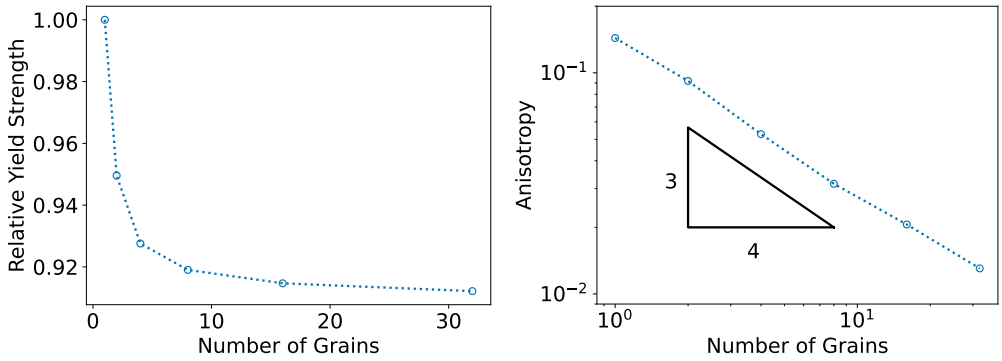

Figure 3-28. Mean yield strength (left) and anisotropy (right) as a function of number of grains.

appear isotropic at a threshold of 10^{-2} or less for the anisotropy measure used here. Again, this suggests that 100μm is an approximate threshold, below which the effects plastic anisotropy should be evaluated for commonly used product forms of structural alloys such as annealed or forged austenitic stainless steel. This threshold assumes an average grain size of 10μm to 50μm, which is generally found in polycrystalline forms of these materials. The analysis here was performed on microstructures with equiaxed grains and uniform texture, so additional study is required to asses changes in the threshold size due to grain geometry and texture. In cases where these effects are pronounced, a strategy very similar to that detailed here should yield the appropriate conclusions with minor adjustments.

4. CONCLUSIONS AND FUTURE WORK

This study suggests that there is an apparent anisotropy observable for a material microstructure with a size on the order of 1 to 10 times the grain size, indicating that microtexture plays a role in the 10μm to 100μm regime for a typical fine-grained alloy. This is significant, and suggests that analysis with relevant length scales on the order of 100μm or less should assess the effects of material anisotropy *even for materials that are effectively isotropic*.

This result suggests more extensive study into the effects of texture as a significant microstructural descriptor. This appears to be especially relevant for accurate simulations of mechanical response for the following reasons. First, some materials and some processing routes tend to produce macrotexture, or the aligning of the crystal orientation throughout a material region of significant extent, or even the entire body. The degree of this texturing controls, among other things, the elastic and plastic anisotropy of the material.

Second, even for materials without macrotexturing, there will always be some length scale over which the material has appreciable texture; here, this length scale is found to be in the neighborhood of 10μm to 100μm. In analysis there is the potential for a loading on a body to introduce a gradient in deformation such that the integral length of this gradient is of the order of this microstructural length scale. Whenever this is the case, the finite element discretization must have elements with characteristic lengths in this regime to accurately capture this gradient. Then, the material in each element is no longer representative of the average material, but has much stronger texture. To date, the impact of this discrepancy remains relatively unquantified, but is almost certainly important, for example, in the run-up to ductile rupture. In order to enhance confidence in the results of this type of analysis, it is necessary to quantify the effects of this discrepancy and develop mitigation strategies when it is demonstrably significant.

For the phenomena studied here, it was found that quantitative measures of material anisotropy and variability of apparent properties all decay with the number of grains in a microstructure, with a scaling exponent between $-1/2$ and $-3/4$. This implies that these quantities decay as the spatial length scale of a calculation to a power between $-3/2$ and $-9/4$. This result can be used, for example, to approximately quantify the effects of apparent anisotropy and microscale variability on quantities of interest in a finite element analysis. This type of approximation can then be used to quantify uncertainty in simulation predictions based on realistic variability in material behavior.

APPENDIX A. Yield criteria

Three invariants of the Cauchy stress tensor are defined as

$$\begin{aligned} I_1 &= \mathrm{tr}(\underline{\underline{\sigma}}) \\ I_2 &= \frac{1}{2}[\mathrm{tr}(\underline{\underline{\sigma}} \cdot \underline{\underline{\sigma}}) - \mathrm{tr}(\underline{\underline{\sigma}})^2] \\ I_3 &= \det(\underline{\underline{\sigma}}) \end{aligned} \tag{A.1}$$

The deviatoric stress is defined as

$$\underline{\underline{s}} = \underline{\underline{\sigma}} - \frac{1}{3} I_1 \underline{\underline{I}} \tag{A.2}$$

The standard invariants of $\underline{\underline{s}}$ are then defined as

$$\begin{aligned} J_1 &= \mathrm{tr}(\underline{\underline{s}}) = 0 \\ J_2 &= \frac{1}{2}[\mathrm{tr}(\underline{\underline{s}} \cdot \underline{\underline{s}}) - \mathrm{tr}(\underline{\underline{s}})^2] = I_2 + \frac{1}{3} I_1^2 \\ J_3 &= \det(\underline{\underline{s}}) = I_3 + \frac{1}{3} I_1 I_2 - \frac{2}{27} I_1^3 \end{aligned} \tag{A.3}$$

The Lode coordinates are given by:

$$\begin{aligned} z &= \frac{1}{\sqrt{3}} I_1 \\ r &= \sqrt{2 J_2} \\ \theta &= \frac{1}{3} \arcsin \left\{ \frac{1}{2} J_3 \left(\frac{3}{J_2} \right)^{3/2} \right\} \end{aligned} \tag{A.4}$$

This coordinate system is convenient for stress analysis, as follows. The π-plane (deviatoric plane) is normal to $\underline{g}_3$ and is spanned by $\underline{g}_1$ and $\underline{g}_2$, with

$$\begin{aligned} \underline{g}_1 &= \frac{1}{\sqrt{2}}[1, 0, -1] \\ \underline{g}_2 &= \frac{1}{\sqrt{6}}[-1, 2, -1] \\ \underline{g}_3 &= \frac{1}{\sqrt{3}}[1, 1, 1] \end{aligned} \tag{A.5}$$

The magnitude of the projection of the principal stress vector $\underline{\sigma} = [\sigma_1, \sigma_2, \sigma_3]$ onto $\underline{g}_3$ is

$$\underline{\sigma} \cdot \underline{g}_3 = \frac{1}{\sqrt{3}} \left(\sigma_1 + \sigma_2 + \sigma_3 \right) = \frac{1}{\sqrt{3}} I_1 = z \tag{A.6}$$

The projection of the principal stress vector $\underline{\sigma} = [\sigma_1, \sigma_2, \sigma_3]$ in the plane normal to $\underline{g}_3$ is

$$\begin{aligned} \underline{\sigma}^{\pi} &= \underline{\sigma} - (\underline{\sigma} \cdot \underline{g}_3) \underline{g}_3 \\ &= [\sigma_1 - \frac{1}{3} I_1, \sigma_2 - \frac{1}{3} I_1, \sigma_3 - \frac{1}{3} I_1] \\ &= [s_1, s_2, s_3] \end{aligned} \tag{A.7}$$

It is clearly seen in (A.7) that any stress vector in the plane normal to $\underline{g}_3$ is purely deviatoric. The vector $\underline{\sigma}$ can be projected onto the orthogonal axes $\underline{g}_1$ and $\underline{g}_2$ of the π-plane to get

$$\begin{aligned} \sigma_1^{\pi} &= \frac{1}{\sqrt{2}} (\sigma_1 - \sigma_3) = \frac{1}{\sqrt{2}} (s_1 - s_3) \\ \sigma_2^{\pi} &= \frac{1}{\sqrt{6}} (-\sigma_1 + 2\sigma_2 - \sigma_3) = \frac{1}{\sqrt{6}} (-s_1 + 2s_2 - s_3) \end{aligned} \tag{A.8}$$

The polar coordinates for the π-plane are then:

$$\begin{aligned} r &= \sqrt{(\sigma_1^{\pi})^2 + (\sigma_2^{\pi})^2} = \sqrt{s_1^2 + s_2^2 + s_3^2} = \sqrt{2 J_2} \\ \theta &= \arctan \left(\frac{\sigma_2^{\pi}}{\sigma_1^{\pi}} \right) = \arctan \left(\frac{1}{\sqrt{3}} \frac{-s_1 + 2s_2 - s_3}{s_1 - s_3} \right) \end{aligned} \tag{A.9}$$

Using (A.8), (A.9), and $s_2 = -(s_1 + s_3)$, the deviatoric principal stresses can then be written as

$$\begin{aligned} s_1 &= \sqrt{\frac{2}{3}} r \cos \left(\frac{\pi}{6} + \theta \right) \\ s_2 &= \sqrt{\frac{2}{3}} r \sin (\theta) \\ s_3 &= -\sqrt{\frac{2}{3}} r \cos \left(\frac{\pi}{6} - \theta \right) \end{aligned} \tag{A.10}$$

From (A.10) the angle θ can be written in terms of the variants J_2 and J_3 as,

$$\theta = \frac{1}{3} \arcsin \left\{ \frac{J_3}{2} \left(\frac{3}{J_2} \right)^{3/2} \right\} \tag{A.11}$$

Thus, the cylindrical axis of (A.4) is parallel to the hydrostatic component of the stress, and the deviatoric components can be plotted in the polar coordinates of the cylindrical cross-section.

A general, quadratic yield condition is given by

$$f\left(\underline{\underline{\sigma}}\right) = \underline{\underline{\sigma}} : \mathbb{Y} : \underline{\underline{\sigma}} - Y^2 = 0 \tag{A.12}$$

For an isotropic material,

$$\mathbb{Y} = a\,\underline{\underline{\mathrm{I}}} \otimes \underline{\underline{\mathrm{I}}} + b\,\mathbb{I}^{\mathrm{sym}} \tag{A.13}$$

For pressure-independent plasticity,

$$a + \frac{1}{3}b = 0 \tag{A.14}$$

so that

$$\mathbb{Y} = b\left(\mathbb{I}^{\mathrm{sym}} - \frac{1}{3}\underline{\underline{\mathrm{I}}} \otimes \underline{\underline{\mathrm{I}}}\right) = b\,\mathbb{I}^{\mathrm{dev}} \tag{A.15}$$

Taking $b = \frac{3}{2}$,

$$\frac{3}{2}\underline{\underline{\sigma}} : \mathbb{I}^{\mathrm{dev}} : \underline{\underline{\sigma}} - Y^2 = 0 \tag{A.16}$$

In terms of the deviatoric stress $\underline{\underline{\mathrm{s}}}$,

$$\frac{3}{2}\underline{\underline{\mathrm{s}}} : \underline{\underline{\mathrm{s}}} - Y^2 = 0 \tag{A.17}$$

That is, the von Mises yield criterion is *the* pressure-independent. isotropic, quadratic yield criterion. Since $\underline{\underline{\mathrm{s}}} : \underline{\underline{\mathrm{s}}} = r^2$, the von Mises yield criterion can be written as

$$r = \sqrt{\frac{2}{3}}Y \tag{A.18}$$

Clearly then, the von Mises yield criterion does not include Lode angle dependence, and including such dependence in an isotropic criterion requires moving beyond a quadratic formulation.

The Tresca yield criterion is given by

$$\begin{gathered} r\cos(\theta^*) = \frac{\sqrt{2}}{2}Y \\ \theta^* = \mathrm{mod}\left(\theta + \frac{\pi}{6}, \frac{\pi}{3}\right) - \frac{\pi}{6}, \quad 0 \le \theta < 2\pi \end{gathered} \tag{A.19}$$

The Hosford yield criterion is given by

$$f(s_1, s_2, s_3) = 2^{-1/n}\left[(s_1 - s_2)^n + (s_1 - s_3)^n + (s_2 - s_3)^n\right]^{1/n} - Y = 0 \tag{A.20}$$

Equation (A.20) can be solved for r given θ using (A.10) to produce a yield criterion in the form of the Tresca (A.19) and von Mises (A.18) above. The cross-sections of the yield surfaces in the π-plane are shown in Figure A-1. There, it can be easily seen that the three criteria agree in general only for states of uniaxial stress.

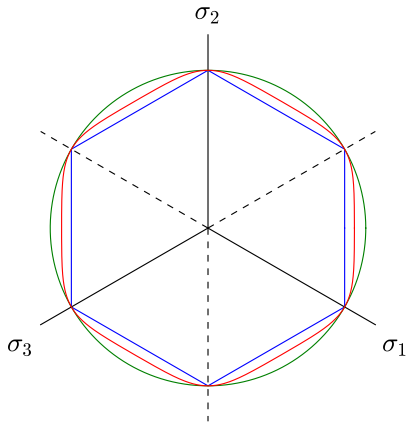

Figure A-1. Cross-sections of the Tresca (blue), von Mises (green), and Hosford, n=10 (red) yield surfaces in the π-plane.

For cubic symmetry,

$$\begin{aligned}\mathbb{Y} = a\sum_{i=1}^{3}\underline{\underline{\underline{\underline{\mathrm{E}}}}}^{(ii)}\otimes\underline{\underline{\underline{\underline{\mathrm{E}}}}}^{(ii)} + \\ b\sum_{i=1}^{3}\sum_{j=1,i\neq j}^{3}\underline{\underline{\underline{\underline{\mathrm{E}}}}}^{(ii)}\otimes\underline{\underline{\underline{\underline{\mathrm{E}}}}}^{(jj)} + \\ c\sum_{i=1}^{3}\sum_{j=1,i\neq j}^{3}\underline{\underline{\underline{\underline{\mathrm{E}}}}}^{(ij)}\otimes\underline{\underline{\underline{\underline{\mathrm{E}}}}}^{(ij)}\end{aligned} \tag{A.21}$$

with

$$\underline{\underline{\underline{\underline{\mathrm{E}}}}}^{(ij)} = \underline{e}^{(i)}\otimes\underline{e}^{(j)} \tag{A.22}$$

For pressure-independent plasticity,

$$a + 2b = 0 \tag{A.23}$$

so that

$$\begin{aligned}\mathbb{Y} = a\left(\sum_{i=1}^{3}\underline{\underline{\underline{\underline{\mathrm{E}}}}}^{(ii)}\otimes\underline{\underline{\underline{\underline{\mathrm{E}}}}}^{(ii)} - \frac{1}{2}\sum_{i=1}^{3}\sum_{j=1,i\neq j}^{3}\underline{\underline{\underline{\underline{\mathrm{E}}}}}^{(ii)}\otimes\underline{\underline{\underline{\underline{\mathrm{E}}}}}^{(jj)}\right) + \\ c\sum_{i=1}^{3}\sum_{j=1,i\neq j}^{3}\underline{\underline{\underline{\underline{\mathrm{E}}}}}^{(ij)}\otimes\underline{\underline{\underline{\underline{\mathrm{E}}}}}^{(ij)}\end{aligned} \tag{A.24}$$

This quadratic formulation introduces a measure of apparent Lode angle dependence, but it turns out not to agree with single crystal yield behavior, as seen in Figure A-2. Even for the best case, where $k = 2$, the best-fit quadratic approximation fails to represent the apparent lode angle dependence of yield strength for a FCC single crystal.

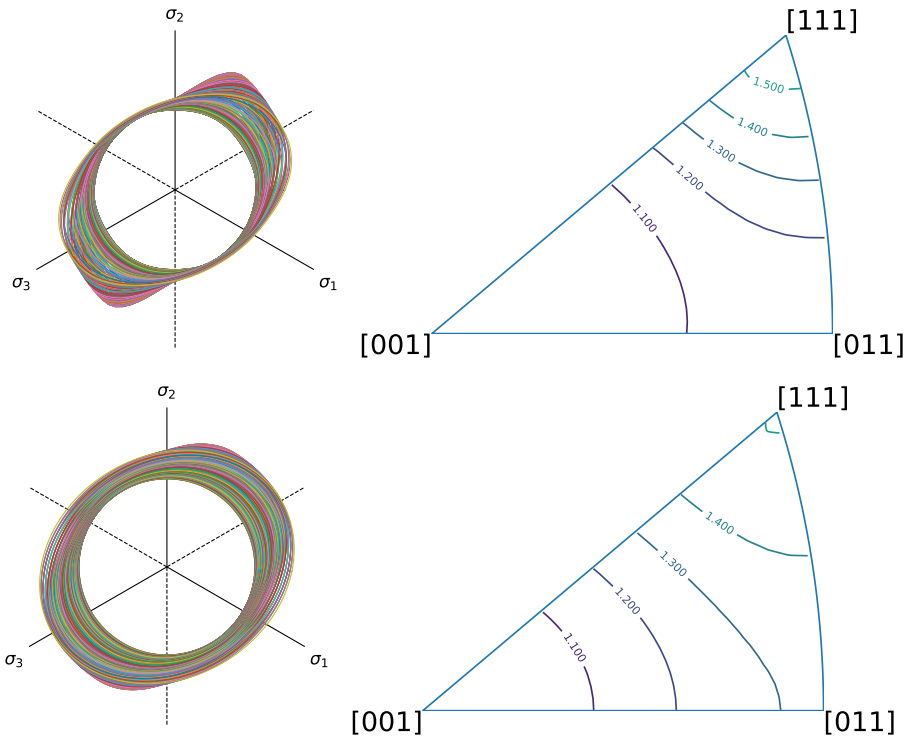

Figure A-2. Comparison of DNS results for yield strength with $k = 2$ (top row) with a quadratic approximation via Equation (A.24) (bottom row). Results are shown as full yield surfaces plotted in the π-plane (left column), and contours of uniaxial yield strength (right column).

APPENDIX B. Alternative yield criteria

A simplified version of single crystal plasticity is examined, where the yield criterion is given by

$$\tau - \tau^{\mathrm{cr}} = \max_{\alpha \in 1,\ldots,N_{\mathrm{slip}}} \left\{ \left| \underline{\underline{\sigma}} : \underline{\underline{\mathrm{P}}}^{\alpha} \right| \right\} - \frac{1}{\sqrt{6}} Y = 0 \tag{B.1}$$

With the crystal aligned with the principal stresses, the single crystal yield cross-section coincides with the Tresca cross-section, as shown in Figure B-1.

For a polycrystal–under the simplifying assumption of uniform stress–adopting the yield criterion:

$$\tau - \tau^{\mathrm{cr}} = \max_{\alpha \in 1,\ldots,N_{\mathrm{slip}}} \left\{ \left| \underline{\underline{\sigma}} : \underline{\underline{\mathrm{P}}}^{\alpha} \right| \right\} - \frac{1}{2} Y = 0 \tag{B.2}$$

recovers Tresca-like behavior, as shown in Figure B-2. This is due to the selection of the weakest link for yielding, which is by definition the single crystal in the aggregate that is most favorably oriented for slip.

If, instead the following criterion is adopted:

$$\begin{gathered} \frac{1}{V} \int \operatorname{sign}(\tau - \tau^{\mathrm{cr}}) dV - V_{\mathrm{cr}} = 0 \\ \tau = \max_{\alpha \in 1,\ldots,N_{\mathrm{slip}}} \left\{ \left| \underline{\underline{\sigma}} : \underline{\underline{\mathrm{P}}}^{\alpha} \right| \right\} \\ \tau^{\mathrm{cr}} = \frac{1}{2} Y \end{gathered} \tag{B.3}$$

that is, yield occurs when a fraction V_{cr} of the material has yielded, the yield surfaces look like those shown in Figure B-3. At low values of V_{cr}, the weakest link is again identified, nearly recovering the Tresca yield criterion. For large values of V_{cr}, the strongest link is identified (and the convexity of the criterion is lost). Neither extreme seems to be physically representative. Following the results in Section 3.2.3, it appears that a value of $V_{\mathrm{cr}} \approx 0.5$ is representative of the DNS results.

Another choice for the definition of the point of plastic yielding is the point at which the plastic power is a given fraction ϕ_{cr} of the total applied power, that is

$$\dot{W}^{p} = \phi_{\mathrm{cr}} \dot{W} \tag{B.4}$$

For plasticity models with a sharp yield point and a physically realistic hardening modulus, under a uniaxial stress state, (B.4) is satisfied when the stress reaches the yield stress. For plasticity

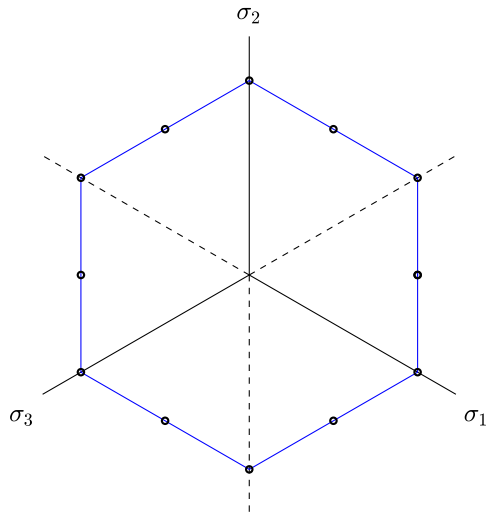

Figure B-1. Cross-sections of the single crystal (solid line) and Tresca (symbols) yield surfaces in the π-plane.

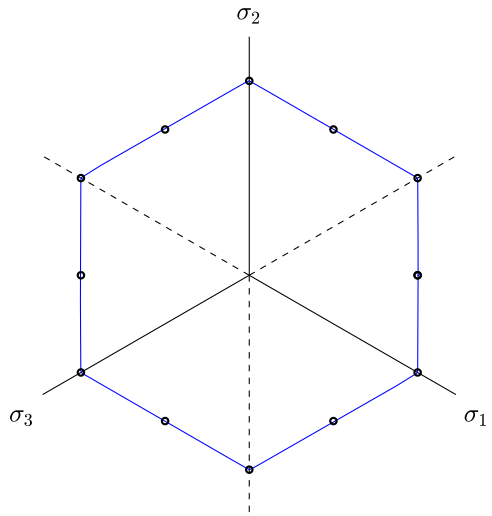

Figure B-2. Cross-sections of the polycrystal yield surface calculated from (B.2) (solid line) and Tresca yield surface (symbols) in the π-plane.

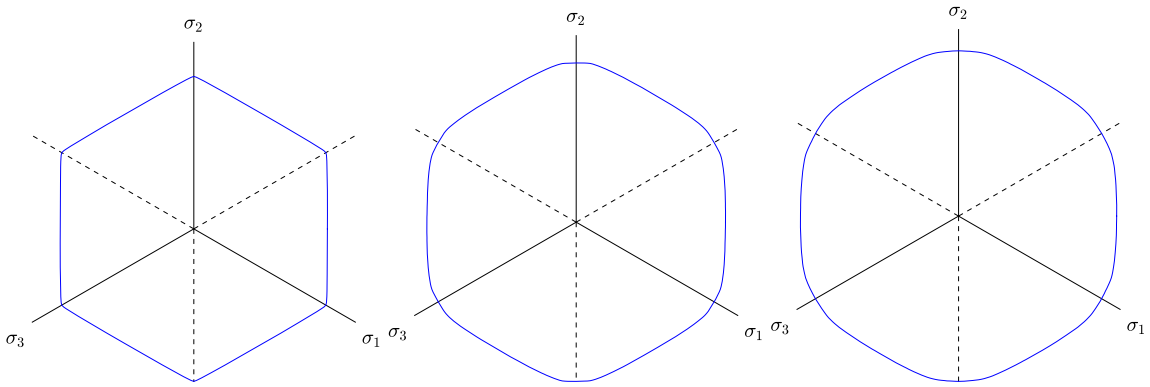

(a) $V_{\text{cr}} = 0.01$ **(b)** $V_{\text{cr}} = 0.3$ **(c)** $V_{\text{cr}} = 0.5$

(d) $V_{\text{cr}} = 0.7$ **(e)** $V_{\text{cr}} = 0.9$ **(f)** $V_{\text{cr}} = 0.99$

Figure B-3. Cross-sections of the polycrystal yield surface calculated from (B.3) **with** $V_{\text{cr}} = \{0.01, 0.3, 0.5, 0.7, 0.9, 0.99\}$ **in the** π**-plane.**

models with a smooth transition from elastic to plastic behavior, as in the microscale model used defined in Section 2.1.2 and summarized here:

$$\begin{aligned}
\underline{\underline{\mathrm{F}}}^{p}(t) &= \int_0^t \underline{\underline{\mathrm{L}}}^{p*}(t') \cdot \underline{\underline{\mathrm{F}}}^{p}(t') dt' \\
\underline{\underline{\mathrm{L}}}^{p*} &= \sum_{\alpha}^{N_{\text{slip}}} \dot{\gamma}^{\alpha} \underline{\underline{\mathrm{P}}}^{\alpha} \\
\dot{\gamma}^{\alpha} &= \left| \frac{\tau^{\alpha}}{g} \right|^{k} \operatorname{sign}(\tau^{\alpha}) \\
\dot{g} &= (H - R_d\, g) \sum_{\alpha}^{N_{\text{slip}}} |\dot{\gamma}^{\alpha}|
\end{aligned} \tag{B.5}$$

(B.4) is satisfied roughly when the apparent hardening rate falls below a critical value. This is a conceptual departure from the historical notion of yield stress defined with a 0.2% offset, which is a criterion based on attaining a critical value of the plastic strain. However, this definition of yield seems intuitive, and it can be used to compare model behavior in a straightforward and physically-motivated way. Varying the value of ϕ_{cr} in (B.4) changes the radius of the yield locus, and changing the value of k in (B.5) changes the shape of the yield locus, as seen in Figure B-4. Lower values of k correspond to lower values of n in Equation (A.20), with n increasing monotonically with k, as seen in Figure B-5.

The analysis of the DNS results in the text above use the criterion (B.4). The DNS-derived yield loci are qualitatively similar to those in Figure B-4, although some differences are expected and observed due to the PDE-governed nature of the DNS problem compared with the algebraic treatment in this Appendix.

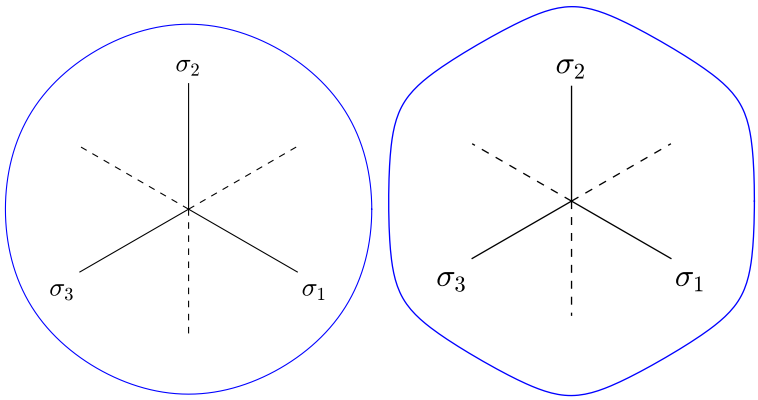

(a) $k = 5$ **(b)** $k = 15$

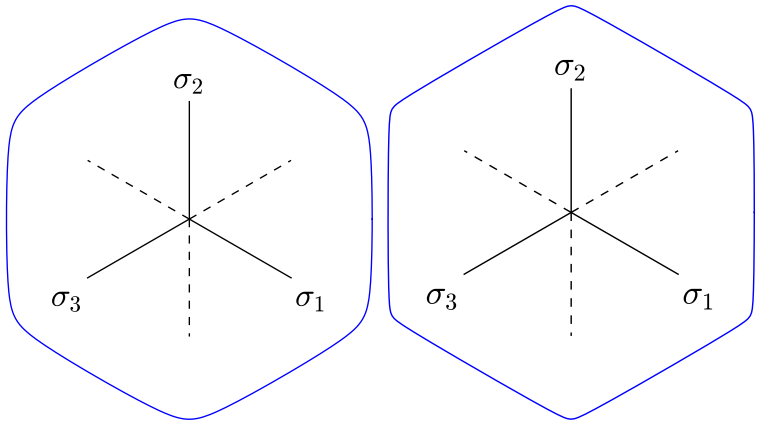

(c) $k = 30$ **(d)** $k = 100$

Figure B-4. Cross-sections of the polycrystal yield surface calculated from (B.4) with $\phi_{\text{cr}} = 0.99$ and $k = 5, 15, 30, 100$ in the π-plane.

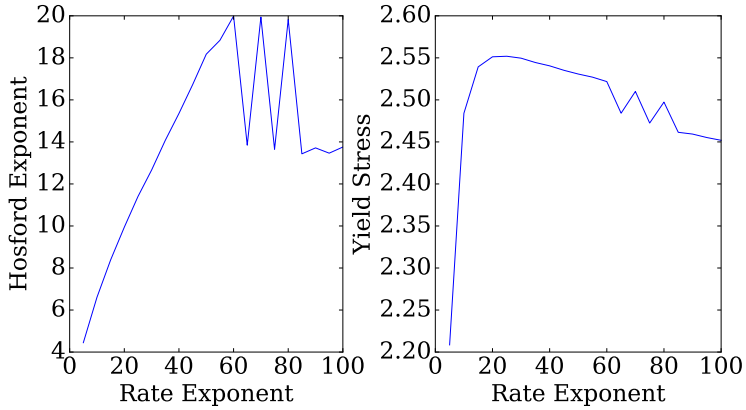

Figure B-5. Hosford parameters (left, n; right, Y) fit to yield loci for specified values $\{5, 10, \ldots, 100\}$ of the rate exponent k in (B.5). Some instability in the fitting procedure is evident for large values of k.

Bibliography

[1] K. Matouš, M. G. D. Geers, V. G. Kouznetsova, and A. Gillman, "A review of predictive nonlinear theories for multiscale modeling of heterogeneous materials," *Journal of Computational Physics*, vol. 330, 2017.

[2] J. E. Bishop, J. M. Emery, R. V. Field, C. R. Weinberger, and D. J. Littlewood, "Direct numerical simulations in solid mechanics for understanding the macroscale effects of microscale material variability," *Computer Methods in Applied Mechanics and Engineering*, vol. 287, pp. 262–289, 2015.

[3] J. E. Bishop, J. M. Emery, C. C. Battaile, D. J. Littlewood, and A. J. Baines, "Direct Numerical Simulations in Solid Mechanics for Quantifying the Macroscale Effects of Microstructure and Material Model-Form Error," *The Journal of the Minerals, Metals, & Materials Society*, vol. 68, no. 5, 2016.

[4] R. Hill, "The Elastic Behaviour of a Crystalline Aggregate," *Proceedings of the Physical Society. Section A*, vol. 65, p. 349, 1952.

[5] J. D. Eshelby, "The Determination of the Elastic Field of an Ellipsoidal Inclusion, and Related Problems," *Proceedings of the Royal Society of London. Series A*, vol. 241, no. 1226, pp. 376–396, 1957.

[6] C. M. Zener, *Elasticity and anelasticity of metals*. Chicago: University of Chicago Press, 1948.

[7] M. Born, "On the stability of crystal lattices. I," *Mathematical Proceedings of the Cambridge Philosophical Society*, vol. 36, no. 2, pp. 160–172, 1940.

[8] M. de Jong, W. Chen, T. Angsten, A. Jain, R. Notestine, A. Gamst, M. Sluiter, C. K. Ande, S. V. D. Zwaag, J. J. Plata, C. Toher, S. Curtarolo, G. Ceder, K. A. Persson, and M. Asta, "Charting the complete elastic properties of inorganic crystalline compounds," *Scientific Data*, vol. 2, p. 150 009, 2015.

[9] F. H. Featherston and J. R. Neighbours, "Elastic Constants of Tantalum, Tungsten, and Molybdenum," *Physical Review*, vol. 130, no. 4, pp. 1324–1333, 1963.

[10] D. I. Bolef, R. E. Smith, and J. G. Miller, "Elastic Properties of Vanadium. I. Temperature Dependence of the Elastic Constants and the Thermal Expansion," *Physical Review B*, vol. 3, no. 12, pp. 4100–4108, 1971.

[11] J. R. Neighbours, F. W. Bratten, and C. S. Smith, "The Elastic Constants of Nickel," *Journal of Applied Physics*, vol. 23, no. 4, pp. 389–393, 1952.

[12] S. M. Collard and R. B. McLellan, "HIGH-TEMPERATURE ELASTIC CONSTANTS OF PLATINUM SINGLE CRYSTALS," *Acta Metallurgica Et Materialia*, vol. 40, no. 4, pp. 699–702, 1992.

[13] J. A. Rayne, “Elastic constants of palladium from 4.2-300°K,” *Physical Review*, vol. 118, no. 6, pp. 1545–1549, 1960.

[14] R. W. Dickson, J. B. Wachtman, and S. M. Copley, “Elastic constants of single-crystal Ni3Al from 10° to 850°C,” *Journal of Applied Physics*, vol. 40, no. 5, pp. 2276–2279, 1969.

[15] K. J. Carroll, “Elastic constants of niobium from 4.2°to 300°K,” *Journal of Applied Physics*, vol. 36, no. 11, pp. 3689–3690, 1965.

[16] H. M. Ledbetter, “Monocrystal-Polycrystal Elastic Constants of a Stainless Steel,” *physica status solidi (a)*, vol. 85, pp. 89–96, 1984.

[17] C. L. Vold, M. E. Glicksman, E. W. Kammer, and L. C. Cardinal, “The elastic constants for single-crystal lead and indium from room temperature to the melting point,” *Journal of Physics and Chemistry of Solids*, vol. 38, no. 2, pp. 157–160, 1977.

[18] S. B. Palmer and E. W. Lee, “The Elastic Constants of Chromium,” *Philosophical Magazine*, vol. 24, no. 188, pp. 311–318, 1971.

[19] Y. A. Chang and L Himmel, “Temperature dependence of the elastic constants of cu, ag, and au above room temperature,” *Journal of Applied Physics*, vol. 37, no. 9, pp. 3567–3572, 1966.

[20] J Vallin, M Mongy, K Salama, and O Beckman, “Elastic constants of aluminum,” *Journal of Applied Physics*, vol. 35, no. 6, pp. 1825–1826, 1964.

[21] R. Hill, “Elastic properties of reinforced solids: Some theoretical principles,” *Journal of the Mechanics and Physics of Solids*, vol. 11, no. 5, pp. 357–372, 1963.

[22] G. Sachs, “Plasticity problems in metals,” *Transactions of the Faraday Society*, vol. 24, pp. 84–92, 1928.

DISTRIBUTION

Email—Internal [redacted]

Name	Org.	Sandia Email Address
Joseph Bishop	1556	jebisho@sandia.gov
Michael Buche	1558	mrbuche@sandia.gov
John Emery	1558	jmemery@sandia.gov
Eliot Fang	1558	hefang@sandia.gov
Kyle Johnson	1558	kyljohn@sandia.gov
Brian Lester	1558	btleste@sandia.gov
Benjamin Reedlunn	1558	breedlu@sandia.gov
William Scherzinger	1558	wmscher@sandia.gov
Corbett Battaile	1864	ccbatta@sandia.gov
Hojun Lim	1864	hnlim@sandia.gov
James Foulk III	8363	jwfoulk@sandia.gov
Alejandro Mota	8363	amota@sandia.gov
Jakob Ostien	8363	jtostie@sandia.gov
Brandon Talamini	8363	btalami@sandia.gov
Kyle Karlson	8752	knkarls@sandia.gov
Technical Library	1911	sanddocs@sandia.gov
CA Technical Library	8551	cateclib@sandia.gov

Sandia National Laboratories

Sandia National Laboratories is a multimission laboratory managed and operated by National Technology & Engineering Solutions of Sandia LLC, a wholly owned subsidiary of Honeywell International Inc., for the U.S. Department of Energy's National Nuclear Security Administration under contract DE-NA0003525.